

# **Small Angle Light Scattering**

## **Analysis of Tissue**

by

**Eric D. Dahlgren**

A Thesis

submitted to the faculty of the

Worcester Polytechnic Institute

in partial fulfillment of the requirements for the

Degree of Master of Science

in Chemical Engineering

---

January 2002

Approved:

---

Prof. Dr. Karen M. McNamara, Advisor

---

Prof. Dr. Ravindra Datta, Department Head

## Summary

Tissue, in particular its mechanical properties, is of interest from a material science point of view. The collagen fiber framework found in nearly all tissue forms the basis for the tissue's behavior. Connective tissue provides more interesting behavior, designed to bear significant load in one direction, while retaining the ability to stretch in other directions. Contributing factors to such behavior are fiber diameter and orientation.

Small angle scattering analysis has been developed over the past century. Particular attention has been paid to x-ray and neutron scattering, both of which characterize features on a nanometer scale. Small angle light scattering (SALS) has the ability to characterize features on a micron scale, and is thus suitable for the analysis of collagen fibers.

Scattering data from several tendons were analyzed using the Generalized Indirect Fourier Transform (GIFT) program developed by Dr. Otto Glatter. The data is fit using cubic B-splines, and transformed into a probability density distribution function (abbreviated PDDF or  $p(r)$ ). The PDDF can then be interpreted to give an average fiber diameter, as well as other structural information.

Since this type of analysis has never been performed on collagen fibers, emphasis was placed on validating small angle light scattering as an appropriate technique to characterize collagen fiber diameter. This was accomplished by comparing the results with optical microscopy. Results from SALS analysis agree with features observed by optical microscopy.

Small angle light scattering analysis is able to provide an analysis of structures superior to that of optical microscopy. Small angle scatter theory provides a three dimensional analysis of the structure. On the other hand, optical microscopy provides only a two dimensional view of the sample. The structure of collagen fibers in tissue is certainly three dimensional, making small angle light scattering a more suitable technique for characterization.

## **Acknowledgements**

I would like to thank the WPI Chemical Engineering faculty for giving me the chance to pursue my education beyond my undergraduate studies. In particular, I'd like to thank my advisor, Professor McNamara, for allowing me to focus on such a diverse research project. Also, the opportunity to work at Johnson Space Center and experience NASA firsthand. I also thank Dr. Anuj Bellare for bestowing some of his light scattering knowledge, and Jack Ferraro for his help tweaking and building various pieces of experimental setup.

Finally, I would like to thank my family and friends for their support over the past years. Without their support, I would not be where I am today. Enjoying what I do, and sometimes flooding the Biopure process development lab.

# Table of Contents

Summary.....	ii
Acknowledgements.....	iv
Table of Figures.....	vii
1. Small Angle Scattering Theory.....	1
1.1 Objective of Small Angle Scattering Analysis.....	1
1.2 Interference of Scattered Waves.....	2
1.3 Scattering Intensity.....	4
1.4 Scattering of Cylindrical Structures.....	5
1.4.1 Resolution of Scattering Components.....	6
1.4.2 Radial and Axial Components in Cylinder Scattering.....	6
1.5 Correlation and Pair Density Distribution Functions.....	8
1.6 Interpreting $p(r)$ .....	9
1.7 The Guinier Approximation.....	10
2. Data Treatment.....	12
2.1 Fitting the Data to Cubic B-splines.....	12
2.2 Determination of Spline Coefficients.....	14
2.3 Fitting Parameters for the Indirect Fourier Transformation.....	16
3. Collagen.....	18
3.1 Amino Acids.....	18
3.1 Molecular Collagen Formation.....	19
3.2 Structure of Collagen Molecules.....	20
3.3 Aggregation of Collagen Molecules.....	22
3.4 Mechanical Properties of Collagen.....	23
3.5 Application of Light Scattering on Collagen Fibers.....	25
4. Experimental Setup.....	28
4.1 Beam Collimation.....	29
4.2 Shrinking the Beam Diameter.....	31
4.3 Experimental Setup Components.....	33

5. Results and Discussion .....	34
5.1 Glatter’s Small Angle Scattering Package.....	34
5.1.1 Validation of Experimental Setup.....	34
5.1.2 File Input.....	36
5.1.3 Data Reduction .....	37
5.1.4 GIFT for Windows.....	37
5.1.5 Validity of GIFT Results .....	39
5.2 Tissue.....	40
5.2.1 Type of Tissue.....	40
5.2.2 Fixation and Sectioning Options.....	41
5.2.3 Applying Loads to the Tendons.....	42
5.3 Data Analysis and Optical Microscopy .....	44
5.3.1 Determination of Average Fiber Diameter .....	45
5.3.2 SALS Results versus Optical Microscopy.....	48
5.3.3 Effect of Stress on Scattering Patterns.....	50
6. Conclusions and Recommendations: Tendons .....	52
7. Articular Cartilage .....	54
7.1 Purpose and Structure .....	54
7.2 Small Angle Scattering Comparison of Healthy and Osteoarthritic Human Articular Cartilage .....	56
8. References.....	60
9. Appendix.....	62
9.1 Cubic B-Spline Program .....	62
9.2 Data Formatting Program .....	67
9.3 Experimental Data and GIFT Results.....	70
9.4 Experimental Procedure.....	83
9.4.1 CASI Alignment .....	83
9.4.2 Data Acquisition .....	84
9.4.3 Tendon Fixation.....	84

## Table of Figures

Figure 1. (left) Interaction between incident laser light and a particle. 1. Incident laser. 2. Particle. 3. Scattered light at angle $\theta$ . 4. Transmitted light. (right) Simulated scattering of a sphere with diameter 20 nm, with $h = 4\pi/\lambda * \sin(\theta/2)$ .....	2
Figure 2. Primary quantities of interest in deriving phase relation between scattered waves $s_1$ and $s_2$ . Here, $h$ is the scattering vector, O and P points where scattering occurs, $r$ the position vector of P, and $s_0$ transmitted light. ....	3
Figure 3. The vector $r$ may be resolved into radial and axial vectors.....	7
Figure 4. (left) $p(r)$ curve from simulated sphere data with diameter 20nm. (right) $p(r)$ curve from simulated cylinder data with cross section diameter of approximately 3nm. ....	10
Figure 5. Set of basis splines created in real space. Only values for $r \geq 0$ are used. ....	14
Figure 6. Choosing the optimal stability parameter, $\lambda_{opt}$ . ....	17
Figure 7. (left) Simulated data (points) and curve fit (line). (right) Once the spline coefficients are known, $p(r)$ can be constructed. Here we see a cylinder of diameter approximately 3 nm and length 13 nm. ....	17
Figure 8. General structure common to all amino acids. The R group is unique to each amino acid.....	18
Figure 9. Condensation reaction that allows the amino acids to form the $\alpha$ chains in a collagen molecule. ....	19
Figure 10. Average dimensions of a collagen molecule (not to scale). The larger dots in the magnified view are glycine residues.....	21
Figure 11. Microfibril formation involves the aggregation of five collagen molecules..	22
Figure 12. Views like this gave rise to the quarter-staggered theory for the arrangement within collagen fibers. Taken from Nimni [1].....	22
Figure 13. Collagen molecules will align such that oppositely charged polar groups (+ and -) and hydrophobic regions (darkened bands) will align, displacing water molecules (black circles).....	23

Figure 14. Typical stress strain curve for tendons (in this case from rat tail) for specimens of different ages. Typical physiological forces fall in the toe region. Taken from Nimni [18].	24
Figure 15. Stress-strain comparison for a collagen molecule (filled circles), collagen fibril (empty circles), and bovine Achilles tendon (empty squares). Taken from Sasaki [21].	25
Figure 16. (left) Typical scattering pattern from collagen fibers showing a high degree of alignment. Fibers will scatter perpendicular to their alignment. (middle) Experimental data from two sheets of collagen fibers with zero degrees between their preferred fiber direction. (right) 52 degrees between preferred fiber directions. Taken from Sacks [6].	26
Figure 17. (left) Original CASI setup. 1. Laser 2. Beam splitter 3. Reference detector 4. Mirror 5. Mirror 6. Spatial filter 7. Concave Mirror. (right) Modified CASI setup.	29
Figure 18. Modified laser housing. The laser (1), beam splitter (2), and reference detector (3) were moved to the top section of the box. The laser now directly exits the box (no mirrors are involved).	30
Figure 19. The collimator, pinhole, and focusing optic (left) are screwed into the spatial filter body (right) to produce a well-defined, collimated beam.	30
Figure 20. (top) The complete experimental setup, minus one of the pinholes. (bottom) experimental setup schematic and beam path. Table is 4 feet by 8 feet.	32
Figure 21. Scattering analysis for 970 nm size latex spheres including the curve fit (left) and $p(r)$ curve (right).	36
Figure 22. Screenshot from the GIFT program showing Lagrange multiplier selection. The mean deviation is near its minimum and $\log N'_c$ near its maximum. The resulting $p(r)$ is displayed in the bottom right.	39
Figure 23. (left) Typical $p(r)$ curve for elongated structures. (right) Although the $p(r)$ curve looks acceptable, the fitting parameters provide a poor representation of the data.	40

Figure 24. Apparatus used to apply loads to the rabbit tendons. Using suture material, the tendon was tied to a post (left). The suture tied to the other end of the tendon was threaded through the plastic wheels and tied to weights. ....	42
Figure 25. Stress-strain curve for rabbit Achilles' tendon [29]. The trend of the curve shows the toe region, where the uncrimping of the fibers causes non-linear behavior. ....	43
Figure 26. Creep test showing the behavior of a rabbit Achilles' tendon under a 0.8 MPa stress [29]. Based on this, tendons loaded for 10 minutes before the addition of glutaraldehyde.....	44
Figure 27. Eight slides were used to take 37 scattering patterns. The general area of each run is indicated.....	44
Figure 28. Raw data comparison of run 17 (right) which could not be adequately fit, with run 16 (left) which was able to be fit. ....	46
Figure 29. Example of fit for raw data (left) and the resulting p(r) curve. The p(r) curve shows an elongated structure with a cross section diameter of 9700 nm. Fitting parameters (run 14) were $D_{max} = 24000$ , $NB = 8$ , and $\lambda = 2.0$ . ....	46
Figure 30. Stained tendon with 40 gram load applied. (a) and (b) are 200x magnification (1mm = 5 microns). (c), (d), and (e) are 400x magnification (1mm = 2.5 microns). ....	48
Figure 31. Stained tendon with 400 gram load applied. (a) and (b) are 200x magnification (1mm = 5 microns). (c), (d), and (e) are 400x magnification (1mm = 2.5 microns). ....	49
Figure 32. Photographs of the scattering created by tendons. From top to bottom, the loads applied were 40, 100, 150, 200, and 400 grams respectively.....	50
Figure 33. Diagram displaying the various regions of articular cartilage and the general orientation of collagen fibrils within each region [34]. ....	55
Figure 34. Micrograph and diagram depicting the shape and distribution of chondrocytes within articular cartilage [34].....	55

Figure 35. Scattering at various azimuthal angles from a section of osteoarthritic articular cartilage where very little collagen is present. (a) articular surface parallel to plane of detection. (b) rotated 30°. (c) rotated 60°. (d) rotated 90° .	56
Figure 36. Scattering at various azimuthal angles from a section of osteoarthritic articular cartilage where collagen is present. (a) articular surface parallel to plane of detection. (c) rotated 30°. (e) rotated 60°. (g) rotated 90° .	57
Figure 37. Scattering at various azimuthal angles from a section of articular cartilage. (a) articular surface parallel to plane of detection. (c) rotated 30°. (e) rotated 60°. (g) rotated 90° .	57
Figure 38. Run 1. Dmax = 24500. NB = 10. $\lambda = 3.5$ .	70
Figure 39. Run 2. Dmax = 24500. NB = 6. $\lambda = 2.5$ .	70
Figure 40. Run 3. Dmax = 24000. NB = 7. $\lambda = 2.5$ .	71
Figure 41. Run 4. Dmax = 23500. NB = 7. $\lambda = 2.5$ .	71
Figure 42. Run 5. Dmax = 21300. NB = 7. $\lambda = 2.0$ .	71
Figure 43. Run 6. Dmax = 22500. NB = 7. $\lambda = 3.0$ .	72
Figure 44. Run 7. Dmax = 19000. NB = 7. $\lambda = 2.5$ .	72
Figure 45. Run 8. Dmax = 22000. NB = 9. $\lambda = 4.0$ .	72
Figure 46. Run 9. Dmax = 23000. NB = 9. $\lambda = 2.5$ .	73
Figure 47. Run 10. Dmax = 26000. NB = 7. $\lambda = 3.5$ .	73
Figure 48. Run 11. Dmax = 19000. NB = 6. $\lambda = 2.5$ .	73
Figure 49. Run 12. Dmax = 22500. NB = 6. $\lambda = 3.0$ .	74
Figure 50. Run 13. Dmax = 21500. NB = 8. $\lambda = 2.5$ .	74
Figure 51. Run 14. Dmax = 24000. NB = 8. $\lambda = 2.0$ .	74
Figure 52. Run 15. Dmax = 22000. NB = 7. $\lambda = 3.0$ .	75
Figure 53. Run 16. Dmax = 27000. NB = 7. $\lambda = 2.0$ .	75
Figure 54. Run 18. Dmax = 22500. NB = 7. $\lambda = 2.5$ .	75
Figure 55. Run 19. Dmax = 17000. NB = 6. $\lambda = 3.5$ .	76
Figure 56. Run 20. Dmax = 21000. NB = 6. $\lambda = 2.5$ .	76
Figure 57. Run 21. Dmax = 18000. NB = 5. $\lambda = 3.0$ .	76

Figure 58. Run 22. Dmax = 18000. NB = 6. $\lambda = 3.5$ .....	77
Figure 59. Run 23. Dmax = 18000. NB = 5. $\lambda = 2.5$ .....	77
Figure 60. Run 24. Dmax = 16500. NB = 5. $\lambda = 3.5$ .....	77
Figure 61. Run 25. Dmax = 21500. NB = 7. $\lambda = 2.5$ .....	78
Figure 62. Run 26. Dmax = 21500. NB = 5. $\lambda = 0.0$ .....	78
Figure 63. Run 27. Dmax = 16000. NB = 7. $\lambda = 3.5$ .....	78
Figure 64. Run 28. Dmax = 22000. NB = 5. $\lambda = 2.0$ .....	79
Figure 65. Run 29. Dmax = 20000. NB = 6. $\lambda = 1.5$ .....	79
Figure 66. Run 30. Dmax = 22000. NB = 6. $\lambda = 3.0$ .....	79
Figure 67. Run 31. Dmax = 24000. NB = 6. $\lambda = 2.5$ .....	80
Figure 68. Run 32. Dmax = 25000. NB = 5. $\lambda = 2.5$ .....	80
Figure 69. Run 33. Dmax = 20000. NB = 5. $\lambda = 3.0$ .....	80
Figure 70. Run 34. Dmax = 23000. NB = 6. $\lambda = 3.0$ .....	81
Figure 71. Run 35. Dmax = 22000. NB = 5. $\lambda = 2.5$ .....	81
Figure 72. Run 36. Dmax = 29000. NB = 7. $\lambda = 2.5$ .....	81
Figure 73. Run 37. Dmax = 20000. NB = 5. $\lambda = 2.5$ .....	82

## 1. Small Angle Scattering Theory

Scattering theory development began in the late 19<sup>th</sup> century. The principle problems being addressed at the time were skylight, its color, and its polarization. The particles being dealt with were much smaller than the incident wavelength (air molecules and sunlight). With continuing advances in both theory and instrumentation, the 20<sup>th</sup> century saw the development of scattering analysis for particles both smaller *and* larger than the incident wavelength [1-5]. Small angle x-ray scattering (SAXS) characterizes features on a nanometer scale. Small angle light scattering (SALS) analysis is very similar to that of SAXS, and sees micron scale features. The following treatment, adapted from Glatter and Kratky's Small Angle X-Ray Scattering, shows the development of some basic SAXS equations. These equations are analogous to SALS equations, except SALS relies on polarizability contrast instead of electron density contrast.

### 1.1 Objective of Small Angle Scattering Analysis

Figure 1 demonstrates what occurs during small angle scatter (SAS). An incident beam of radiation interacts with some type of dielectric inhomogeneity. Some of the incident beam is transmitted, while some is scattered. Physically, the incident laser light causes oscillating dipoles, which in turn emit light (of the same wavelength as the incident beam) in all directions. Since the source for each scattered wave occurs at a different point in space, interference between these scattered waves occurs. The objective of small angle scatter theory is to correlate the intensity of the scattered light

measured at various angles relative to the incident light to some physically meaningful quantity.

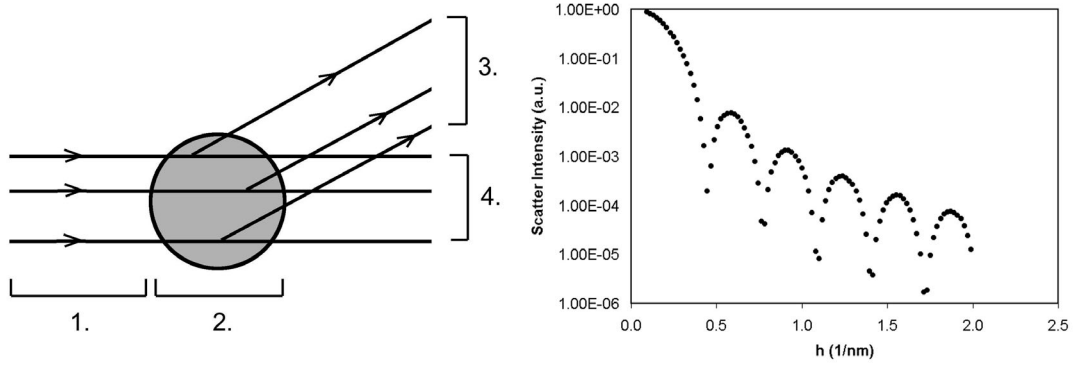


Figure 1. (left) Interaction between incident laser light and a particle. 1. Incident laser. 2. Particle. 3. Scattered light at angle  $\theta$ . 4. Transmitted light. (right) Simulated scattering of a sphere with diameter 20 nm, with  $h = 4\pi/\lambda * \sin(\theta/2)$ .

## 1.2 Interference of Scattered Waves

Consider the following case. Incoming incident light is being scattered at two points, separated by vector  $r$  (one of these points being an arbitrarily assigned origin, O). Figure 2 shows the quantities of interest. Each secondary (scattered) wave can be represented by  $e^{i\phi}$ , where  $\phi$  is the phase relationship of light scattering at point P. The mathematical representation for this difference is

$$\phi = \frac{2\pi}{\lambda}(s_1 - s_0)(-r) \quad (1)$$

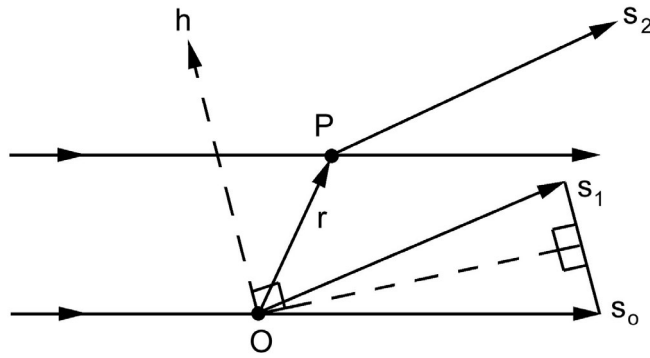


Figure 2. Primary quantities of interest in deriving phase relation between scattered waves  $s_1$  and  $s_2$ . Here,  $h$  is the scattering vector,  $O$  and  $P$  points where scattering occurs,  $r$  the position vector of  $P$ , and  $s_0$  transmitted light.

where

- $\phi$  = phase difference, radians
- $\lambda$  = incident wavelength, nm
- $s_0$  = unit vector in direction of incident beam, dimensionless
- $s_1$  = unit vector in direction of scattered light, dimensionless
- $r$  = vector relating origin to any point in space, nm

Since  $(s_1 - s_0)$  is symmetric with respect to the transmitted and scattered light from the origin, it can be rewritten using the angle created by the scattered and transmitted light ( $\theta$ ).

$$(s_1 - s_0) = 2 \sin\left(\frac{\theta}{2}\right) \quad (2)$$

where

$$\theta = \frac{1}{2} \text{ the angle between } s_1 \text{ and } s_0, \text{ radians}$$

The scattering vector,  $h$ , can be written as  $(4\pi/\lambda)\sin(\theta/2)$ . As can be seen in figure 2, the scattering vector has the same direction as  $(s_1-s_0)$ . The phase relation between waves scattered at different points as  $\phi = -hr$ .

### 1.3 Scattering Intensity

One of the assumptions upon which this development is based is the coherence of the scattered waves. This means that amplitudes can be added, and intensities can be found by taking the absolute square of the sum of amplitudes. Given the large number of atoms (hence elements that create contrast in x-ray or light scattering), a density of these elements,  $\rho(r)$ , can be created. In x-ray scattering, these elements would be electrons. In light scattering, dielectrics (non-conductors) would make up the elements. In a unit volume,  $dV$ , an integral gives the sum of all secondary waves as a function of scattering vector:

$$F(h) = \int_V \rho(r) e^{-ihr} \cdot dV \quad (3)$$

where

$$\begin{aligned} F(h) &= \text{amplitude of scattered wave at } h, \text{ dimensionless} \\ \rho(r) &= \text{scattering element density, number/nm}^3 \\ V &= \text{unit volume, nm}^3 \end{aligned}$$

The amplitude is the Fourier transform of the density distribution. The intensity is simply the square of the absolute value of the amplitude. Multiplying equation (3) by its complex conjugate  $F^*$  (which will have the same magnitude), leads to the following:

$$FF^* = \iint \rho(r_1)\rho(r_2) e^{-ih(r_1-r_2)} \cdot dV_1 \cdot dV_2 \quad (4)$$

where

$F^*$  = complex conjugate of  $F$ , dimensionless

Separating this equation into two integrals will help give physical meaning to it. The first integral is known as the auto-correlation operation, and is shown below.

$$\bar{\rho}^{-2}(\mathbf{r}) = \int \rho(\mathbf{r}_1)\rho(\mathbf{r}_2)dV_1 \quad (5)$$

where

$$\bar{\rho}^{-2}(\mathbf{r}) = \text{auto-correlation, number/nm}^3$$

Here,  $r$  represents a constant, and is equal to  $(r_1-r_2)$ . The second integral performed is

$$I(\mathbf{h}) = \int \bar{\rho}^{-2}(\mathbf{r}) \cdot e^{-i\mathbf{h}\cdot\mathbf{r}} \cdot dV \quad (6)$$

where

$I(\mathbf{h})$  = intensity at  $\mathbf{h}$ , dimensionless

This is also a Fourier transform. From equation (6), it can be clearly seen that the scattering pattern is due solely to the contributions of equation (5), which is in turn determined by the structure of what is being observed. As shown by Debye [6], the exponential in equation (6) may be replaced by its average over all directions of  $\mathbf{r}$ .

$$\langle e^{-i\mathbf{h}\cdot\mathbf{r}} \rangle = \frac{\sin(\mathbf{h}r)}{\mathbf{h}r} \quad (7)$$

#### 1.4 Scattering of Cylindrical Structures

When dealing with a structure that is elongated in one or two directions (such as cylinders and lamella, respectively), certain alterations to data treatment occur. Since this

work deals with analyzing collagen fibers, which are assumed to be elongated in one direction, only the alterations for cylinders are discussed.

### 1.4.1 Resolution of Scattering Components

Consider a rectangular parallelepipedon. The amplitude of scattered light can be split into three factors, one for each axis, if the vector  $r$  in equation (3) is replaced by  $(x\alpha + y\beta + z\gamma)$ . Here  $x$ ,  $y$ , and  $z$  represent the Cartesian coordinates, and  $\alpha$ ,  $\beta$ , and  $\gamma$  represent a unit vector in the direction of  $h$ . Other assumptions include a dilute solution (so only scattering from single particles need be considered), a center of symmetry, constant particle density, and constant solvent density. The symmetry condition allows the phase factor to be written as  $\cos(hr)$ . After integration, equation (3) becomes

$$F(\mathbf{h}) = (\Delta n_e) \frac{\sin(ha\alpha)}{ha\alpha} \frac{\sin(hb\beta)}{hb\beta} \frac{\sin(hc\gamma)}{hc\gamma} \quad (8)$$

where

- $a, b, c$  = Cartesian coordinates
- $\alpha, \beta, \gamma$  = unit vector in direction of  $h$
- $\Delta n_e$  = volume \*  $\Delta\rho$
- $\Delta\rho$  = scattering element density difference

As can be seen, each of the sign terms represents factors from each of the Cartesian axes.

### 1.4.2 Radial and Axial Components in Cylinder Scattering

Applying the same procedure to cylinders is quite similar, except that only two vectors, axial and radial, are required to describe a location. Figure 3 gives a graphic

representation of these quantities, where the vector  $\mathbf{r}$  can be written as the sum of  $z$  and  $r_c$ .

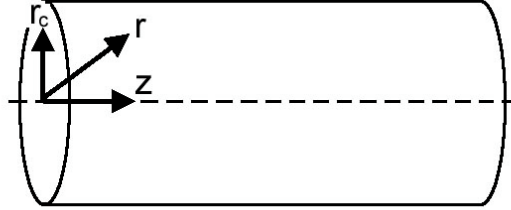


Figure 3. The vector  $\mathbf{r}$  may be resolved into radial and axial vectors.

The integral of equation 3 now becomes

$$F(\mathbf{h}) = (\Delta\rho) \cdot L \frac{\sin(hL\gamma/2)}{(hL\gamma/2)} \cdot \int e^{-i\mathbf{h}\cdot\mathbf{r}_c} dA \quad (9)$$

where

$L$  = length of cylinder, nm

$\gamma$  = cosine of angle between  $\mathbf{h}$  and  $z$ -axis, dimensionless

The terms containing  $L$  and the integral represent contributions to the amplitude from length and cross sectional area respectively. Since one of the assumptions of this development is that there is elongation in the  $z$  direction ( $L$  is large), then the axial factor drops to zero rapidly as the angle between  $\mathbf{h}$  and the  $z$ -axis strays from  $90^\circ$ . The physical meaning of this being contributions to the scattering pattern occur only when the cylinder is perpendicular to  $\mathbf{h}$ . It is helpful to think of  $\mathbf{h}$  as being contained in the plane that the detector goes through while taking experimental data.

Whereas three dimensions were able to be factored in the analysis of the parallelepipedon, only one dimension can be factored out in the analysis of the cylinder. This leaves the integral defined over an area. Previously, the average phase factor for three-dimensional analysis was given by equation (7). This equation must be altered, since the analysis is now in two dimensions. The resulting equation is

$$\langle e^{-ihr_c} \rangle = J_0(hr_c) \quad (10)$$

where  $J_0$  is the zero-order Bessel function

$$J_0(x) = 1 - \frac{x^2}{[2^2 * (1!)^2]} + \frac{x^4}{[2^4 * (2!)^2]} - \dots \quad (11)$$

## 1.5 Correlation and Pair Density Distribution Functions

The goal of this development is to relate  $I(h)$  to some physically meaningful quantity. The function  $p(r)$ , a density distribution of the vector  $r$ , can be interpreted to give a maximum and average dimension (such as particle or fiber diameter). To get  $p(r)$  from the experimental data, one final quantity must be introduced,  $\gamma(r)$ . This function is known as the correlation function, and is defined as

$$\gamma(r) = \langle \eta(r_1)\eta(r_2) \rangle \quad (12)$$

where

$$\begin{aligned} r &= |r_1 - r_2|, \text{ nm} \\ \eta(r) &= \rho(r) - \bar{\rho}, \text{ number/nm}^3 \\ \bar{\rho} &= \text{average scattering element density, number/nm}^3 \end{aligned}$$

The purpose of  $\eta(r)$  is to subtract out the large background that makes no contribution to the scattering pattern. Though Glatter's text makes no reference to the mathematics behind the next substitution, equation (6) is now written as

$$I(h) = V \int \gamma(\mathbf{r}) \cdot e^{-i\mathbf{h}\mathbf{r}} \cdot dV \quad (13)$$

To get an equation for  $p(r)$ , the following equations are used [1,7]

$$p(r) = r^2 \gamma(r) \quad (14)$$

$$p_c(r) = r\gamma(r) \quad (15)$$

for spherical and cylindrical geometries, respectively. This is the mathematical relation between experimental data,  $I(h)$ , and the distance distribution function,  $p(r)$ .

## 1.6 Interpreting $p(r)$

Interpretation of the  $p(r)$  function is not difficult. For spherical geometry, the  $p(r)$  curve will intersect the  $r$ -axis when  $r$  is equal to the diameter of the structure. The  $p(r)$  curve for spheres has been solved analytically [7], and is given below.

$$p(r) = 12x^2(2 - 3x + x^3) \quad (16)$$

where

$$\begin{aligned} x &= r/D, \text{ dimensionless length} \\ D &= \text{sphere diameter, nm} \end{aligned}$$

For cylindrical geometry, the diameter of the cylinder occurs at an inflection point in the  $p(r)$  curve. Examples of each  $p(r)$  curve are given in figure 4. Although from equations (14) and (15) it seems  $p(r)$  should equal zero at  $r$  equal to zero, this is not a necessary

condition when analyzing data. Deviations can be attributed to any background scatter not completely subtracted from the experimental data.

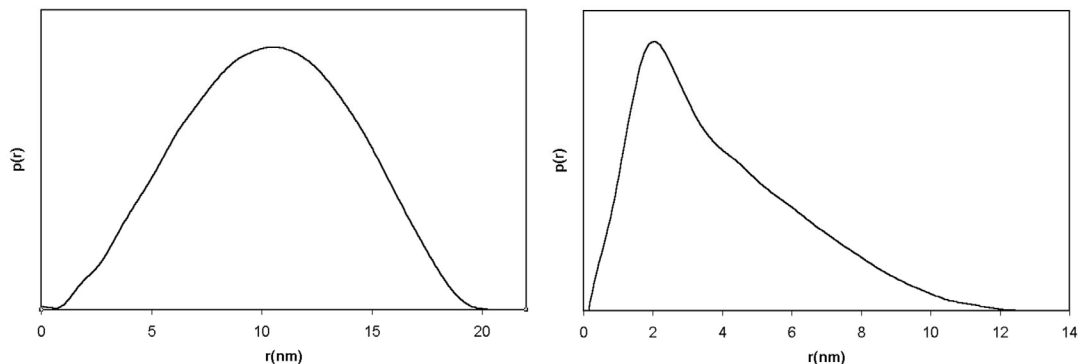


Figure 4. (left)  $p(r)$  curve from simulated sphere data with diameter 20nm. (right)  $p(r)$  curve from simulated cylinder data with cross section diameter of approximately 3nm.

The cylindrical  $p(r)$  in figure 4 is generated making no assumptions about shape (i.e. equation 14 is used). Should scattering data be analyzed to take into account elongation in one direction, the  $p(r)$  curve for a circular cylinder would resemble that of a sphere. When data is analyzed in such a manner,  $p(r)$  is generally changed to  $p_c(r)$ . The subscript “c” denotes “cross section.” The diameter of the cylinder is where  $p_c(r)$  intersects the r-axis.

### 1.7 The Guinier Approximation

The Guinier Approximation is based on the notion that all structures can be described by a “radius of gyration” parameter. Similar to the radius of gyration of mass found in basic physics, the connotation is now that of polarizability in light scattering and electron density in x-ray scattering.

Scattering amplitude of a single oriented particle can be written as

$$F(\mathbf{h}) = (\Delta\rho) \int \cos(\mathbf{h}\mathbf{r}) dV \quad (17)$$

Cos (hr) can be expanded into the following power series:

$$\cos(\mathbf{h}\mathbf{r}) = 1 - \frac{(\mathbf{h}\mathbf{r})^2}{2} + \dots \quad (18)$$

The integral in equation 17 now becomes

$$V \left\langle 1 - \frac{(\mathbf{h}\mathbf{r})^2}{2} + \dots \right\rangle \quad (19)$$

where the average is taken at fixed h over all r. To get intensity from amplitude (intensity is the square of the amplitude), all orientations (or r) must be averaged together. As seen in section 1.4.1, hr can be replaced with  $h\langle x\alpha + y\beta + z\gamma \rangle$ . The average square for  $\alpha, \beta$ , and  $\gamma$  are all equal to 1/3, and the sum of the average squares of x,y, and z is equal to the average of r squared. Using these rules and algebraic manipulation, the intensity can be written as follows:

$$I(\mathbf{h}) = V^2 (\Delta\rho^2) \left( 1 - \frac{h^2 \overline{r^2}}{3} + \dots \right) \quad (20)$$

The power series term can be replaced with its exponential equivalent, giving the well-known Guinier Approximation.

$$I(\mathbf{h}) = V^2 (\Delta\rho^2) e^{-h^2 R^2 / 3} \quad (21)$$

## 2. Data Treatment

There are two approaches to analyzing data. The experimental data can be fit to a known scattering model, or a model free approach can be used [8]. This work deals with the latter approach, in particular the methods developed by Otto Glatter [9]. Ideally, to get from an experimental scattering curve to a probability density distribution function ( $p(r)$  curve), one would need data from a scattering vector of zero to infinity. Anything less would lead to termination effects in the Fourier transform. Intensity at zero angle is not attainable because the incident beam intensity is magnitudes larger than the scattering intensity. Intensity at larger angles shows increasing noise in the data (as well as it being physically impossible to collect data beyond  $180^\circ$ ). The most current version of Glatter's analysis program is known as GIFT (Generalized Indirect Fourier Transform).

### 2.1 Fitting the Data to Cubic B-splines

Representation of the data as the sum of cubic-B splines has been shown an effective technique for fitting and transforming the data [10-12]. Each individual spline is non-zero only over a span of four knots. We begin by assuming that the particles being observed have some maximum distance  $D$ . Therefore  $p(r \geq D) = 0$ , and we only need spline functions to represent data over the finite range zero to  $D$ . This leads to the equation

$$p_A(r) = \sum_{v=1}^N c_v \phi_v(r) \quad (22)$$

where

$$\begin{aligned} p_A(r) &= p(r) \text{ approximation, dimensionless} \\ c_v &= \text{coefficient of spline } v \\ \varphi_v(r) &= \text{spline } v \end{aligned}$$

The Fourier transform of each spline may be taken and represented as  $\psi_v(h)$ , such that

$$I_A(h) = \sum_{v=1}^N c_v \psi_v(h) \quad (23)$$

where

$$\begin{aligned} I_A(h) &= \text{scattering approximation, dimensionless} \\ \psi_v(h) &= \text{Fourier transform of } \varphi_v(h), \text{ dimensionless} \end{aligned}$$

with

$$\psi_v(h) = 4\pi \int_0^{D_{\max}} r \cdot \varphi_v(r) \cdot \frac{\sin(hr)}{h} \cdot dr \quad (24)$$

The experimental data is fitted to these splines, using a weighted least squares routine. Figure 5 shows a set of basis splines (spline coefficients  $c_v$  all equal to 1) for  $D_{\max} = 13$  and number of splines equal to 15. The splines were created using code written in Microsoft Visual Basic 6.0. The subroutines BVALUE and INTERV from de Boor [13] were used in the program, which dumped the data points to a formatted text file. The complete code can be found in the appendix. It is worthy of note that Glatter's use of basis splines evolved since his first paper [9]. Originally, the splines were used to represent a radial density profile,  $\rho(r)$ , as opposed to the probability density distribution function. This was for the program ITRO. Later, the splines were used to represent  $p(r)$

in the programs ITP and GIFT. Now, a separate program (DECON) calculates the radial density profile by a deconvolution of  $p(r)$ .

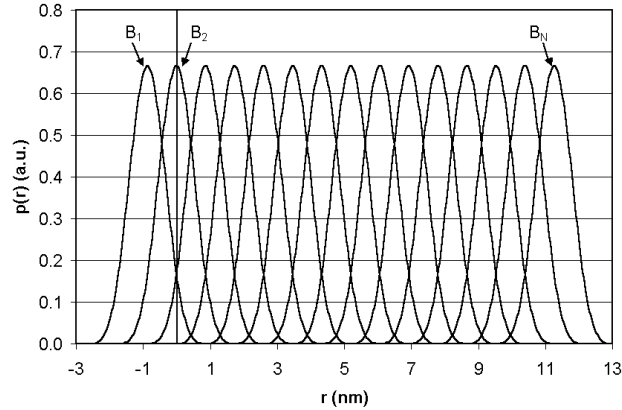


Figure 5. Set of basis splines created in real space. Only values for  $r \geq 0$  are used.

## 2.2 Determination of Spline Coefficients

The following condition is used to calculate the unknown spline coefficients:

$$L = \sum_{i=1}^M [I_{\text{exp}}(h_i) - \sum_{v=1}^N c_v \psi_v(h_i)]^2 / \sigma^2(h_i) = \min \quad (25)$$

where

$M$  = number of data points

$N$  = number of splines

$h_i$  = data point  $i$ ,  $\text{length}^{-1}$

$I_{\text{exp}}(h_i)$  = experimental intensity at  $h_i$ , dimensionless

$\sigma^2(h_i)$  = variance at point  $h_i$ , dimensionless

The solution to this is given by the system

$$\mathbf{B}_{\mu\nu}\mathbf{c}_\nu = \mathbf{d}_\mu \quad \mu, \nu = 1, 2, \dots, N \quad (26)$$

$$\mathbf{B}_{\mu\nu} = \sum_{i=1}^M \psi_\mu(\mathbf{h}_i)\psi_\nu(\mathbf{h}_i) / \sigma^2(\mathbf{h}_i)$$

$$\mathbf{d}_\mu = \sum_{i=1}^M \mathbf{I}_{\text{exp}}(\mathbf{h}_i)\psi_\mu(\mathbf{h}_i) / \sigma^2(\mathbf{h}_i)$$

Stability issues may arise due to the size of  $N$ , and the error within the data. To aid in attaining a solution, a stability parameter  $\lambda$  is introduced. Equation 25 is rewritten

$$\mathbf{L} + \lambda \mathbf{N}_{c'} = \min \quad (27)$$

$$\mathbf{N}_{c'} = \sum_{\nu=1}^{N-1} (\mathbf{c}_{\nu+1} - \mathbf{c}_\nu)^2$$

Consequently, equation 26 becomes

$$(\mathbf{B}_{\mu\nu} + \lambda \mathbf{K}_{\mu\nu})\mathbf{c}_\nu = \mathbf{d}_\mu \quad (28)$$

with matrix  $\mathbf{K}$  equal to

$$\mathbf{K} = \begin{pmatrix} 1 & -1 & & & & \\ -1 & 2 & -1 & & & \\ & & \ddots & & & \\ & & & -1 & 2 & -1 \\ & & & & -1 & 1 \end{pmatrix}$$

### 2.3 Fitting Parameters for the Indirect Fourier Transformation

The three primary parameters involved in fitting the data are the number of spline functions (NB), the stabilization parameter ( $\lambda$ ), and  $D_{\max}$  (about 1.5~2 times the largest distance in the particle). Enough splines functions must exist to correctly approximate  $p(r)$  and the experimental data; however, large values of N can lead to stability problems. Typically, N is less than 30. Once a  $D_{\max}$  and N are chosen, the system is solved using a range of stabilization parameters. The optimum value,  $\lambda_{\text{opt}}$ , is chosen where the function  $N_c(\lambda)$  shows an inflection point (or plateau) and the mean deviation per point is at a minimum, as shown in figure 6 (taken from GIFT screen). Finally, the spline fit and  $p(r)$  curves are generated. Figure 7 demonstrates the creation of  $p(r)$  for a cylinder using the basis splines shown in figure 5, and also shows the raw data and curve fit. Scattering data was simulated using Glatter's Multibody program and analyzed with the GIFT program.

As a consequence of the sampling theorem [14-16], there exists a limit on how large a value of  $D_{\max}$  can be chosen in relation to the range of data collected.

$$D_{\max} \leq \frac{\pi}{h_1} \quad (29)$$

where  $h_1$  is the smallest angle where data collection begins. Violation of this inequality will lead to increased oscillations in the  $p(r)$  function. Starting analysis at the smallest possible cutoff angle will not necessarily lead to better results [17], since structures may not exist that scatter at such a small angle; however, data should be collected in this range so an appropriate  $h_1$  can be determined later on in the analysis process.

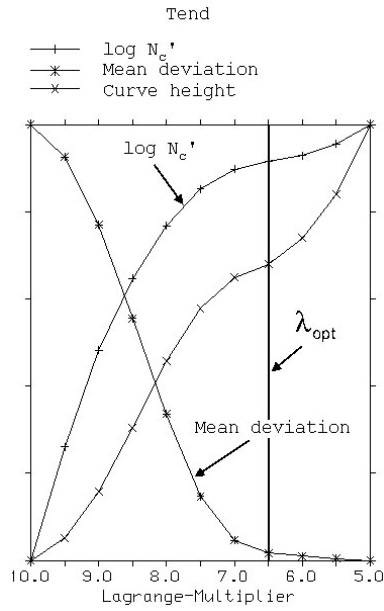


Figure 6. Choosing the optimal stability parameter,  $\lambda_{opt}$ .

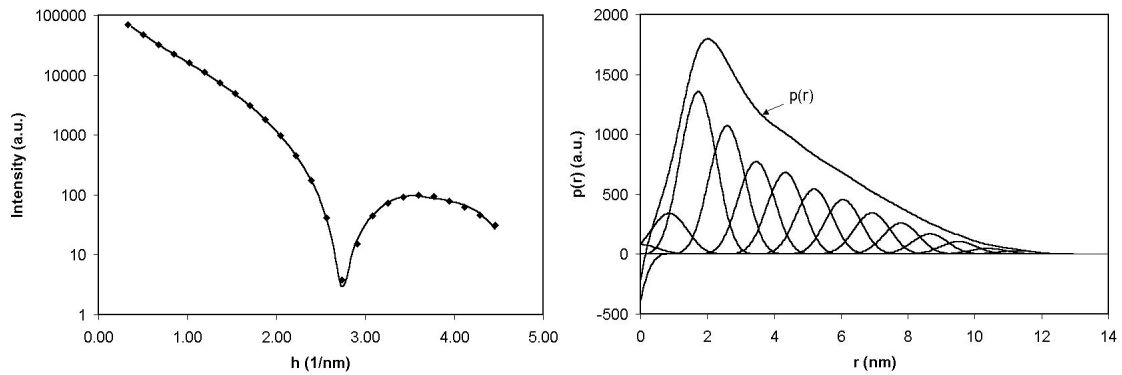


Figure 7. (left) Simulated data (points) and curve fit (line). (right) Once the spline coefficients are known,  $p(r)$  can be constructed. Here we see a cylinder of diameter approximately 3 nm and length 13 nm.

### 3. Collagen

Collagen is the substance responsible for holding the body together, and is made up of long chains of amino acids (also known as proteins). It can be found in any of 12 forms. Connective tissue, which includes ligaments and tendons, contains mostly type I collagen. Collagen comprises 65-75% of the dry mass of tendon. Articular cartilage, on the other hand, contains primarily type II collagen (approximately 50% dry mass). Type I and II collagens differ in their arrangement of the amino acid chains. The type and size of collagen fibers can vary widely from tissue to tissue; however, the overall trend is that tissue requiring higher tensile strength requires thicker fibers. Tissue requiring elasticity will have a greater number of thinner fibers. The following background contains highlights from Nimni's *Collagen* series [18], which contains many references to the more esoteric issues involved.

#### 3.1 Amino Acids

All amino acids have a common structure. Attached to a carbon atom are an amine group, carboxyl group, hydrogen atom, and a side chain unique to each amino acid (see figure 8).

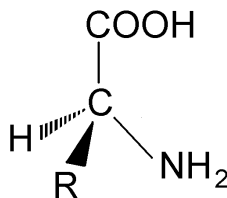


Figure 8. General structure common to all amino acids. The R group is unique to each amino acid.

When in solution, the carboxyl group (acidic) will donate its hydrogen to the amine group (basic). Glycine, the most abundant amino acid in a collagen molecule, simply has a hydrogen atom in the R group.

The ability to link together is what allows amino acids to form the chains necessary to make the  $\alpha$  chains in a collagen molecule. The carboxyl group from one amino acid will undergo a condensation reaction with the amine group from another amino acid, as shown in figure 9. This results in a peptide bond (carbon to nitrogen).

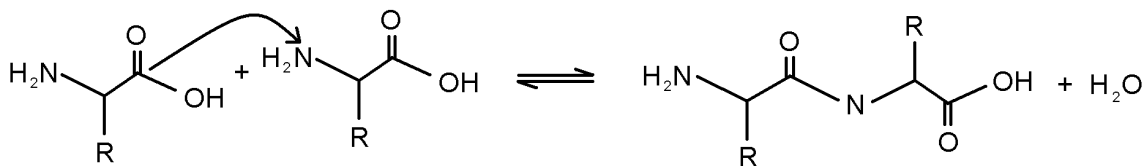


Figure 9. Condensation reaction that allows the amino acids to form the  $\alpha$  chains in a collagen molecule.

### 3.1 Molecular Collagen Formation

Collagen formation (fibrillogenesis) begins with messenger RNA (mRNA) inside cells known as fibroblasts. Fibroblasts are found throughout the body, allowing collagen production (including specific types) to be produced where needed. Each type of collagen (more specifically each type of  $\alpha$  chain, of which each collagen molecule contains three) has its own mRNA gene. An  $\alpha$  chain begins formation at one end of the mRNA molecule, and is known as a pro- $\alpha$  chain until completed. The pro- $\alpha$  molecule is

moved along the mRNA while continuing to build a particular sequence of amino acids until the end of the gene is reached.

Once three pro- $\alpha$  chains have been created they are cleaved from the mRNA and all joined at one end by sulfur bridges. These three chains then twist, forming the collagen triple helix (a completely thermodynamically driven process). The molecule (which is still not quite collagen due to chains on the ends of the molecule) is then brought to the edges of the cell and expelled. This is where unnecessary chains are cleaved from the ends of the molecule. All of these building and cleaving processes are completely enzyme driven. Three of the more prominent enzymes involved are prolyl hydroxylase, prolyl 3-hydroxylase, and lysyl hydroxylase.

### **3.2 Structure of Collagen Molecules**

Nearly all of the more than 20 amino acids can be found in any given type of  $\alpha$  chain. A few types of amino acids are found in large numbers. Table 1 shows typical amounts of each amino acid per 1000 residues [19]. A residue equals one amino acid. Every 3<sup>rd</sup> residue in the sequence is glycine, a distance of approximately 8.7 Å. The large amount of glycine is a significant factor in the coiled nature of the collagen molecule. The triple helix makes one complete twist approximately every 86 Å. One collagen molecule has a diameter of 1.5 nm and length of 300 nm. These dimensions are shown in figure 10. Type I collagen contains two  $\alpha$ 1(I) chains and a single  $\alpha$ 2(I) chain. Type II collagen contains three  $\alpha$ 1(II) chains. The Roman numeral in parentheses indicates what

type of collagen is being described. The Arabic numeral indicates a particular type of chain in the collagen molecule (in case of more than one type).

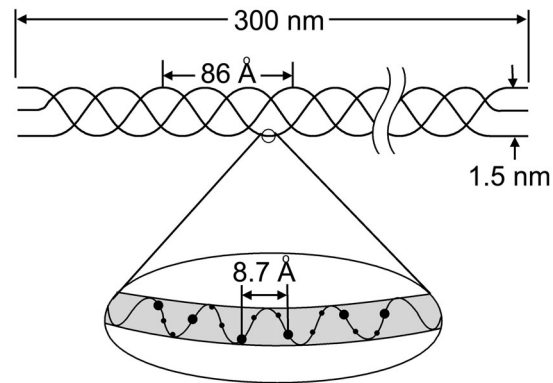


Figure 10. Average dimensions of a collagen molecule (not to scale). The larger dots in the magnified view are glycine residues.

Table 1. Human collagen composition. Type appears in parentheses.

Amino Acid	$\alpha 1(I)$	$\alpha 2(I)$	$\alpha 1(II)$
Glycine	333	338	333
Proline	124	113	120
Alanine	115	102	103
4-Hydroxyproline	108	93	97
Glutamic Acid	73	68	89
Arginine	50	50	50
Aspartic Acid	42	44	43
Serine	34	30	25
Lysine	26	18	15
Valine	21	35	18
Leucine	19	30	26
Threonine	16	19	23
Phenylalanine	12	12	13
Hydroxylysine	9	12	20
Methionine	7	5	10
Isoleucine	6	14	9
Histidine	3	12	2
3-Hydroxyproline	1	1	2
Tyrosine	1	4	2
Gal-hydroxylysine	1	1	4
Glc-gal-hydroxylysine	1	2	12
Half-cystine	0	0	0

### 3.3 Aggregation of Collagen Molecules

The next step toward fiber formation is the aggregation of collagen molecules. The first step is the formation of microfibrils. A microfibril, or at least the more generally accepted view, is a group of five collagen molecules (see figure 11). It is the simplest subunit able to create the quarter-staggered arrangement, which will be discussed soon. The pioneers in developing this model were Hodge, Petruska, and Smith [19,20]. From here, the five member microfibrils aggregate in both an end-to-end and stacking fashion to form a collagen fiber. When stained, the fibers show a repeating pattern of striations. These striations are a result of how the microfibrils join together to form a quarter-staggered arrangement (see figure 12).

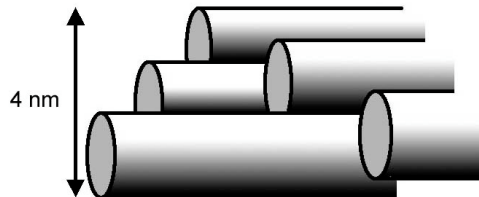


Figure 11. Microfibril formation involves the aggregation of five collagen molecules.

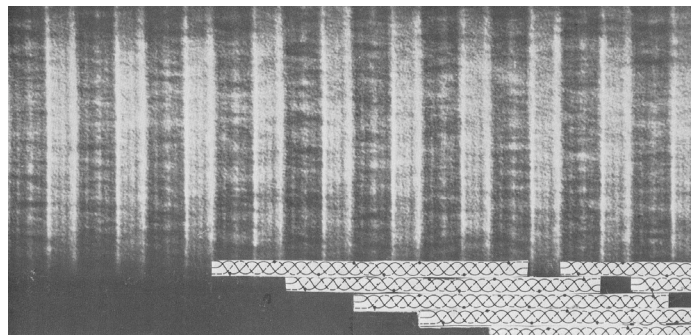


Figure 12. Views like this gave rise to the quarter-staggered theory for the arrangement within collagen fibers. Taken from Nimni [1].

The various amino acids (and their associated polar groups and hydrophobic nature) are the driving force behind these patterns. The collagen molecules (and microfibrils) align such that the polar groups attract each other. This also allows for any water molecules near the hydrophobic sites to be “squeezed out” from between two converging collagen molecules, as shown in figure 13.

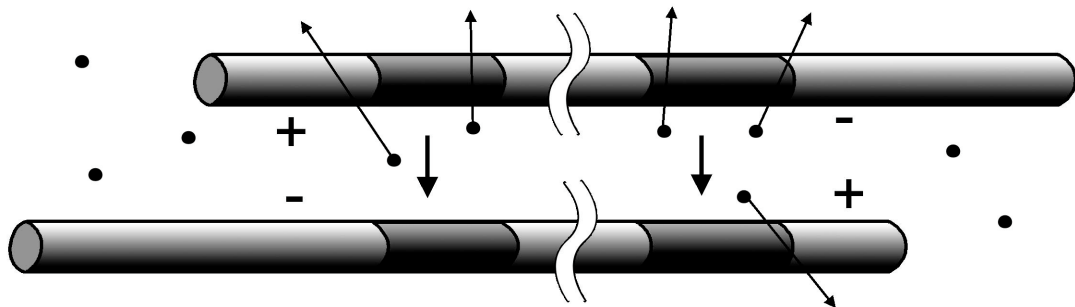


Figure 13. Collagen molecules will align such that oppositely charged polar groups (+ and -) and hydrophobic regions (darkened bands) will align, displacing water molecules (black circles).

### 3.4 Mechanical Properties of Collagen

The most useful information about the mechanical properties of collagen can be found in its stress-strain curve. Stress is the amount of force applied per unit area, while strain measures the amount of deformation (or lengthening) relative to an arbitrary starting size. Figure 14 gives an example of a typical stress-strain curve, and the different regions. The region corresponding to normal physiological operating range is the toe region. The linear (elastic) region is where Young’s modulus is calculated, and

elongation is reversible. The yield (plastic) regions are where permanent deformation and damage occur.

Recent efforts have focused on elucidating contributions to mechanical properties from different structural levels of collagen [21,22]. Figure 15 shows Sasaki's experimental stress-strain curve for a collagen molecule, a collagen fibril, and tendon. It is worth noting that the collagen molecule and collagen fibril show only linear behavior. The tendon, however, shows the typical toe region, due to the uncrimping of the fibers, followed by a linear region. The linear region of the tendon shows nearly the same slope as the fibril.

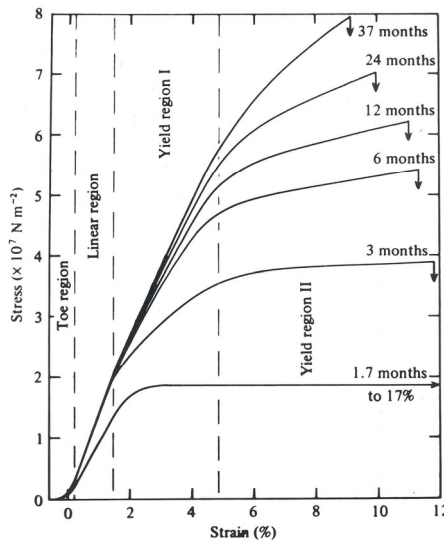


Figure 14. Typical stress strain curve for tendons (in this case from rat tail) for specimens of different ages. Typical physiological forces fall in the toe region. Taken from Nimni [18].

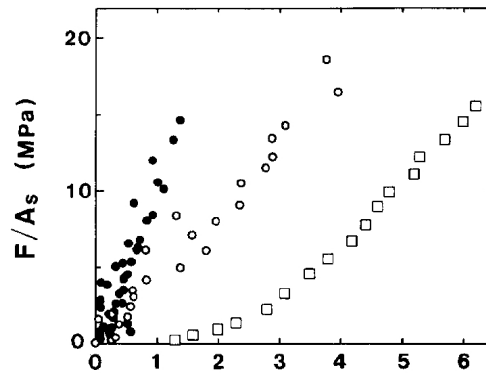


Figure 15. Stress-strain comparison for a collagen molecule (filled circles), collagen fibril (empty circles), and bovine Achilles tendon (empty squares). Taken from Sasaki [21].

### 3.5 Application of Light Scattering on Collagen Fibers

Light scattering has been used to characterize fiber orientation [23], and also correlate orientation to biaxial loading properties of porcine intestinal submucosa and a collagenous repair biomaterial [24,25]. Fiber orientation describes how fibers are arranged with respect to one another within a tissue. Tendons have highly aligned fibers since they are designed to bear significant load in only one direction. Skin, on the other hand, has random fiber orientation since it needs to bear loads in many directions. Data was collected using a CCD camera, and scattering intensity plotted as a function of azimuthal angle,  $\Phi$  (see figure 16). The primary objectives were to map the fiber architecture of tissue, which can be bimodal in some cases. Bimodal orientations aid in bearing loads in more than one direction. Using Sacks' analysis, unimodal and bimodal orientations can be distinguished, as seen in figure 16.

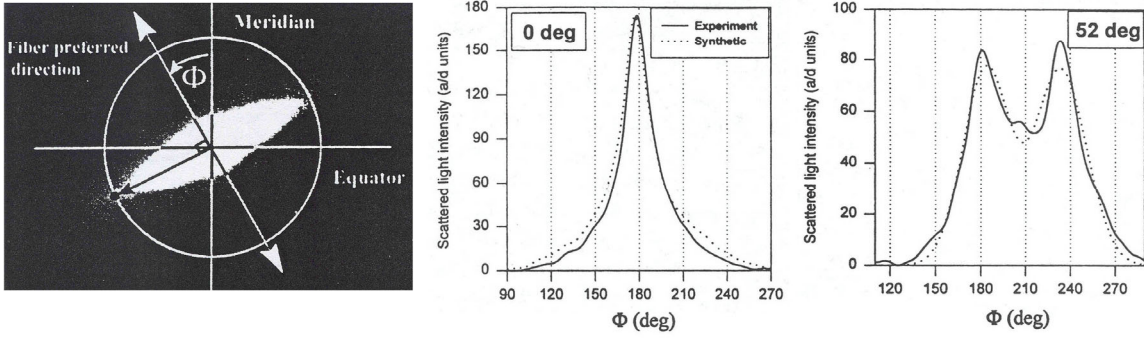


Figure 16. (left) Typical scattering pattern from collagen fibers showing a high degree of alignment. Fibers will scatter perpendicular to their alignment. (middle) Experimental data from two sheets of collagen fibers with zero degrees between their preferred fiber direction. (right) 52 degree between preferred fiber directions. Taken from Sacks [6].

Light scattering analysis can take many forms, including the use of diffraction theory [26], as shown by Ferdman and Yannas. Once again, data was collected using a CCD camera. Normal dermis was compared to scar tissue, in terms of both fiber diameter and orientation. Using equation 30, an average fiber diameter was obtained. The results obtained compared well with optical microscopy, falling within the ranges of experimental error. Since data was recorded using a CCD camera, an orientation analysis was performed using equation 31 ( $\Phi$  in figure 16). For completely random orientations, S will equal zero. For perfectly aligned fibers, S will equal 1. They were able to show that the dermis contained random oriented fibers, while scar tissue showed a high degree of alignment.

$$d = \frac{\lambda}{\sin \theta} \tag{30}$$

where

$d$  = average fiber diameter, nm  
 $\lambda$  = incident wavelength, nm  
 $\theta$  = first minimum in scattering intensity, radians

$$S = 2 \frac{\int_0^{\pi/2} I(\beta) \cos^2 \beta d\beta}{\int_0^{\pi/2} I(\beta) d\beta} - 1 \quad (31)$$

where

$S$  = orientation index, dimensionless  
 $I(\beta)$  = intensity at angle  $\beta$ , dimensionless  
 $\beta$  = azimuthal angle, radians

The major drawback with this type of analysis is the intensity never reaches an obvious first minimum, but has an exponential-like decay. This makes the determination of theta, and fiber diameter, less than definitive. However, their results compared well with optical microscopy and confirm that light scattering is well suited to collagen fibers.

#### **4. Experimental Setup**

The experimental setup uses a modified Schmitt Measurement Systems, Inc. Scatterometer [27]. Scattered light is measured using a detector called CASI (Complete Angle Scatter Instrument). Data is collected in the form of power density versus angle. While no modifications to the detector were required, there were changes made to other sections of the system in order to maximize signal and reduce the beam size to an acceptable diameter. Higher beam intensity will allow for more signal at higher angles, where noise starts to become prevalent. Tissue samples were as small as 1mm in some directions; therefore, the beam had to be smaller to prevent artifacts from the edges of the tissue.

The laser source is a Melles-Griot Helium-Neon (HeNe) laser with a wavelength of 632.8 nm (red). The power output is 7 mW minimum, and 10 mW maximum. The beam is linearly polarized. The initial configuration is shown in figure 17. The beam coming out of the housing is conical shaped (converging). The housing is a box with dimensions of approximately 20" high by 32" long by 7" deep. The detector (which did not require modification) is mounted on a rotating arm. The detector element is made of silicon. There are four choices for aperture sizes, with 3977 microns used to acquire data in this work.

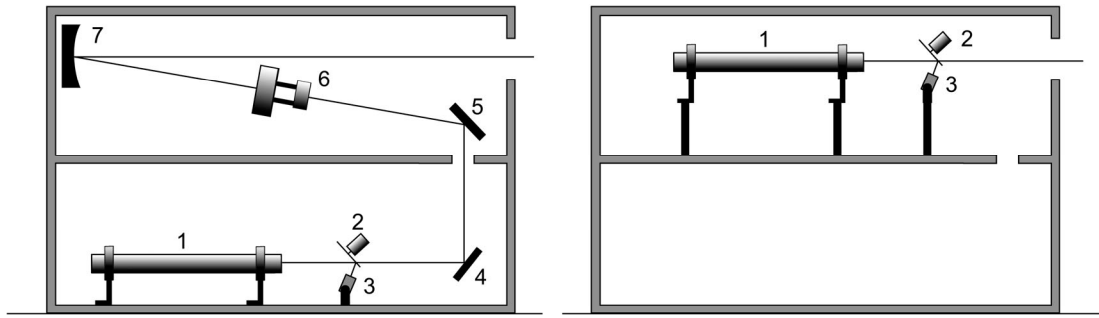


Figure 17. (left) Original CASI setup. 1. Laser 2. Beam splitter 3. Reference detector 4. Mirror 5. Mirror 6. Spatial filter 7. Concave Mirror. (right) Modified CASI setup.

#### 4.1 Beam Collimation

The first task was collimating the beam. Attempts to use a single lens (outside the laser housing) proved fruitless. The beam hitting the concave mirror off axis caused distortion that prevented collimation of any quality. After many rounds of trial and error, all the mirrors and the spatial filter were removed. The laser, beam splitter, and reference detector were then moved to the upper section of the box (see figure 17), and a new system of optical components created outside the box. An added benefit of this modification is increased signal. Anytime a mirror redirects the laser, intensity is lost due to scatter.

The spatial filter provided by Schmitt Measurement Systems was replaced with a Melles-Griot spatial filter, which allowed the attachment of a collimator (see figure 19). The spatial filter, through the use of a focusing optic and pinhole, blocks stray beams of light. The focusing optic is a 16 mm convex lens. The pinhole has a diameter of 25 microns. The focusing optic creates a diverging beam. In order to compensate for this, a

collimator is attached to the end of the spatial filter. The collimator has an adjustable focus from a few meters to infinity.

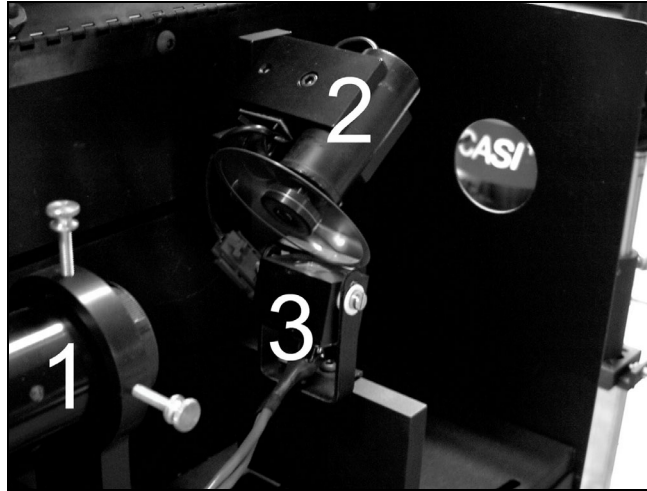


Figure 18. Modified laser housing. The laser (1), beam splitter (2), and reference detector (3) were moved to the top section of the box. The laser now directly exits the box (no mirrors are involved).

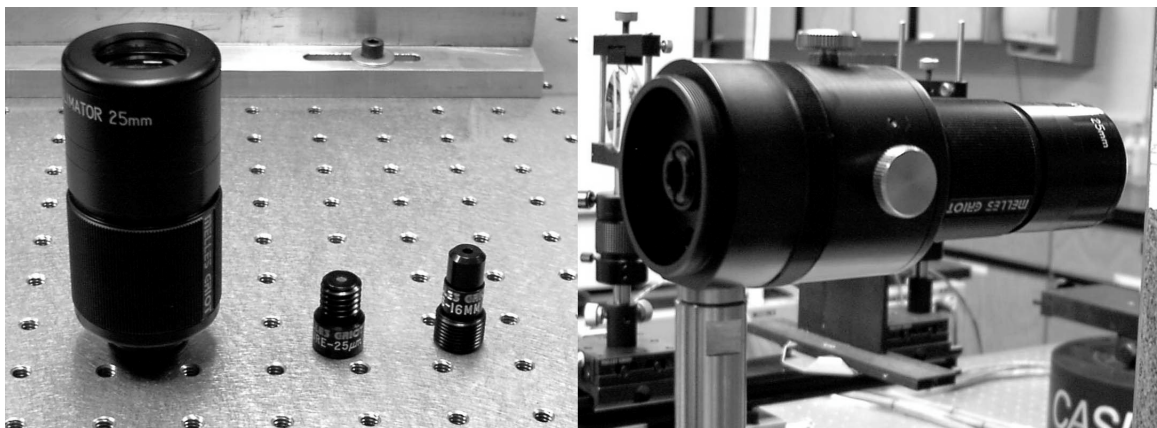


Figure 19. The collimator, pinhole, and focusing optic (left) are screwed into the spatial filter body (right) to produce a well-defined, collimated beam.

## 4.2 Shrinking the Beam Diameter

Two mirrors are used to reflect the beam a distance of a few meters so other optics can be placed within the range of the collimator's focusing range. These adjustable mirrors also serve the purpose of correcting the height of the beam, such that the beam is parallel with the table at the height of the detector.

The beam then travels through a system of lenses and pinholes to create a well-defined beam at a small diameter ( $< 1$  mm). Initial attempts included using a beam expander in the reverse direction, but alignment proved impossible. Instead, individual beam expander lenses were used. They were mounted on adjustable height rods, as well as a translation stage for alignment purposes. These were then mounted onto an optical rail using two sliding mounts. These sliding mounts allowed the space between the lenses to be adjusted to produce a highly collimated beam.

The purpose of the pinholes is to reduce the stray radiation created by reflected laser light. Although the two lenses used to shrink the diameter of the beam have anti-reflective coatings, they are hardly adequate. As such, one pinhole is placed between the two lenses on the optical mount. The other pinhole is placed right next to the sample (on the side opposite the detector). The entire setup (minus the pinhole between the two lenses, for easier viewing) is shown in figure 20.

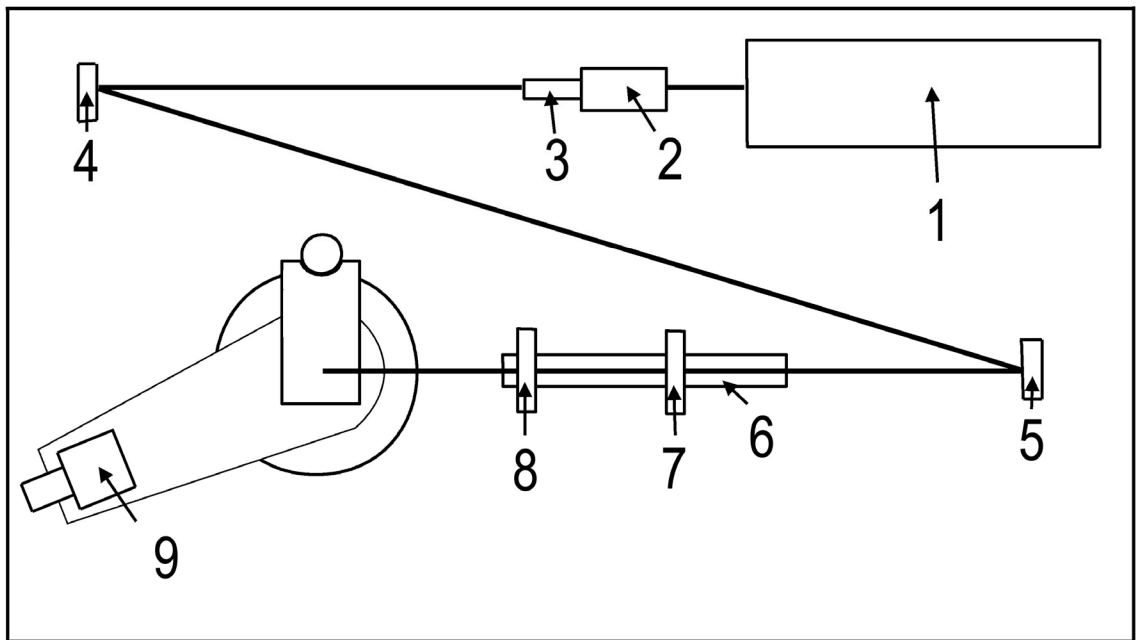
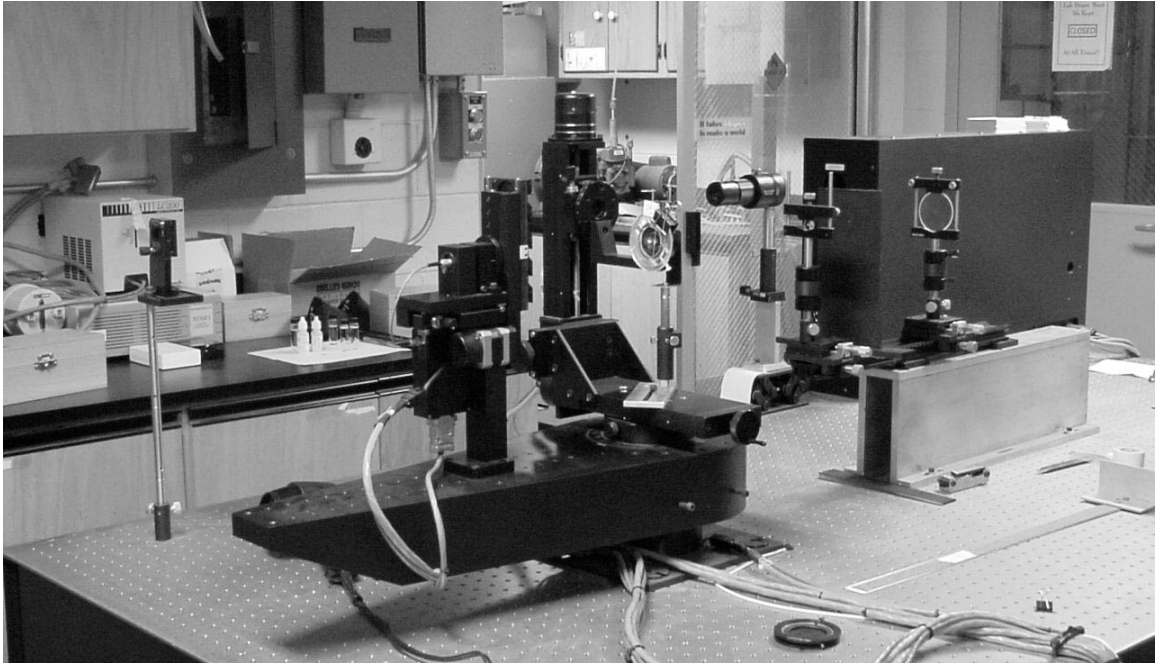


Figure 20. (top) The complete experimental setup, minus one of the pinholes. (bottom) experimental setup schematic and beam path. Table is 4 feet by 8 feet.

### 4.3 Experimental Setup Components

The part numbers of pieces found in the experimental setup (as seen in the schematic in figure 20) are as follows:

All pieces are from Melles-Griot.

1. Laser source – 05-LHP-171
2. Spatial filter – 09-LSF-011  
Focusing optics – 09-LSL-009  
Pinhole – 09-LSP-023
3. Collimator – 09-LCM-011
4. Mirror – 02-MLQ-011/023
5. Mirror – 02-MLQ-015/023
6. Optical rail – 07-ORN-003
7. Lens – 01-LBX-005 (output lens)
8. Lens – 01-LBX-001 (output lens)
9. Detector

## **5. Results and Discussion**

Constructing and refining the experimental setup occupied a majority of the time spent on this work, and the promising results obtained have made all that work worthwhile. These results are the most important aspect of this work. Once the experimental setup reached completion, some type of validation was necessary. In the past, small angle light scattering was successfully applied to scattering from latex spheres [28]. This seemed an appropriate method to test the performance of the experimental setup and demonstrate the application of Glatter's analysis package.

### **5.1 Glatter's Small Angle Scattering Package**

The small angle scattering suite of programs is a powerful analysis tool. PDH2000 is a data manipulation tool, allowing for such operations as averaging files, subtracting files, or data reduction. GIFT for Windows analyzes scattering data, creating a pair density distribution function. DECON for Windows takes the  $p(r)$  curve and creates a radial scattering profile. Multibody can simulate scattering curves of various structures by representing them with a combination of smaller spheres.

#### **5.1.1 Validation of Experimental Setup**

970 nanometer spheres were chosen to test the new setup because they scatter in a range suited to the incident wavelength. Previous experiments took extensive measures to ensure scattering data was extremely accurate. Beam stops and index matching baths were employed to effectively eliminate reflections and stray radiation. Highly purified

water eliminated contaminants. Since this work was not meant to validate or test these methods, a simple cylindrical cuvette and deionized water were used. Figure 21 shows the raw data, and is qualitatively very similar to latex sphere scattering patterns obtained in previous work [28]. Thus the contributions of reflections and stray radiation so diligently minimized in previous work appears to have been inconsequential in this instance.

Initial attempts to fit the data were not completely successful. The low  $h$  section of the scattering data was not being represented correctly, most likely due to multiple scattering. The fit was continually underestimating the data, no matter what parameters were used. Multiple scattering is caused by incident light scattering off one sphere, and the scattered light scattering from a different sphere. Diluting the sample solves the problem of multiple scattering, but this solution was unacceptable. The sample had already been diluted as much as possible while still retaining an acceptable signal to noise ratio at higher angles. These circumstances necessitated the use of a structure factor in the GIFT program to help fit the data [29,30]. The incorporation of a structure factor helps account for contributions to the scattering pattern caused by multiple scattering. Figure 21 shows the resulting fit and  $p(r)$  curve. A structure factor was only needed in this instance. Tendon data did not require a structure factor to achieve an adequate fit, which may be due to the sectioning thickness of 10 microns. At most, there could be one layer of collagen fibers since preliminary optical microscopy showed fibers on the order of 10 microns. This would aid in the elimination of multiple scattering.

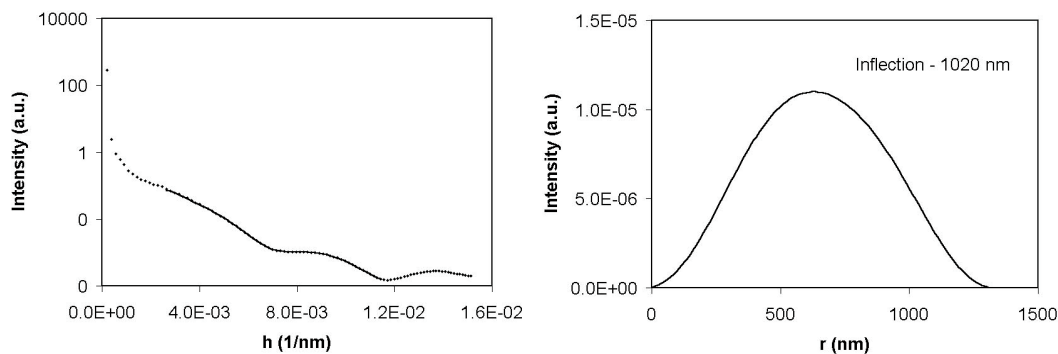


Figure 21. Scattering analysis for 970 nm size latex spheres including the curve fit (left) and  $p(r)$  curve (right).

The  $p(r)$  curve inflection indicates an average diameter of 1020 nm, which is close to the actual size of 970 nm and within experimental error. The general  $p(r)$  shape indicates a spherical structure, but the curve does indicate show some degree of deformity with the maximum dimension around 1400 nm. Overall, these results show our experimental setup capable of producing accurate scattering data similar to theoretical scattering patterns (see figure 1).

### 5.1.2 File Input

The original ITP algorithms and code required a strict input format. This strict input format has carried over into GIFT. In order to facilitate analyzing the CASI data, a program was written in Visual Basic to transform the experimental data from the CASI format to the GIFT format (see appendix).

### **5.1.3 Data Reduction**

Once the data is in the format required by GIFT, data reduction may be required. Given the radius of the detector and aperture size, small angular increments were needed to ensure the entire scattering range was covered. With a large angular increment, there will be angles not represented in the data. Once the data has been collected, the large number of data points is not necessary. Data reduction is used to fit the trend of the data as opposed to the noise, especially at higher angles where signal can easily fall below noise levels. Tendon data was reduced using the “binning” feature of PDH2000. For scattering vectors less than 0.003, a compression factor of 3 was used. For scattering vectors greater than 0.003, a compression factor of 4 was used. These settings allowed for a fairly even distribution of points across reciprocal space. The interpolation option was used in the binning procedure. Without this option enabled, fitting the data using GIFT was impossible. Sphere data was compressed by a factor of two using the interpolation option, and no adverse effects were seen. Interpolation uses an alternate method to calculate standard deviation at a point.

### **5.1.4 GIFT for Windows**

For GIFT to analyze the data, certain input parameters are required. These include the range of data points to be fit, the range of Lagrange multipliers calculated, the maximum r-value, and the number of splines. The starting point and maximum r-value are loosely related by equation 24 as seen in section 2.3. While a minor violation of this equation does violate the sampling theorem, it does not completely invalidate the results

[17]. The maximum  $r$ -values for the tendons generally fall between 20,000 and 23,000 nm. The starting  $h$ -value generally fell between 0.0002 and 0.0004. Lagrange multipliers were calculated from 8.0 to 0.0 in 0.5 decrements. The number of splines generally fell in the range of 5 to 9. There is no direct method for determining working values. Trial and error must be employed.

Once all the input parameters have been entered and the calculations completed, a Lagrange multiplier must be selected. Ideally, the multiplier will be selected where  $N'_c$  from equation 22 shows an inflection point and the mean deviation per point is at a minimum. Unless the system is ideal (dilute and monodisperse), this condition will not be obtained. Figure 22 shows how Lagrange multipliers for tendon data were chosen.

From here, the solution is saved and several output files are created. The most useful are \*.app, \*.por, and \*.IO\$. Files with the extension “app” contain the curve fit. Files with the extension “por” contain the  $p(r)$  data points. Finally, files with the extension “IO\$” contain the spline coefficients used to create the solutions.

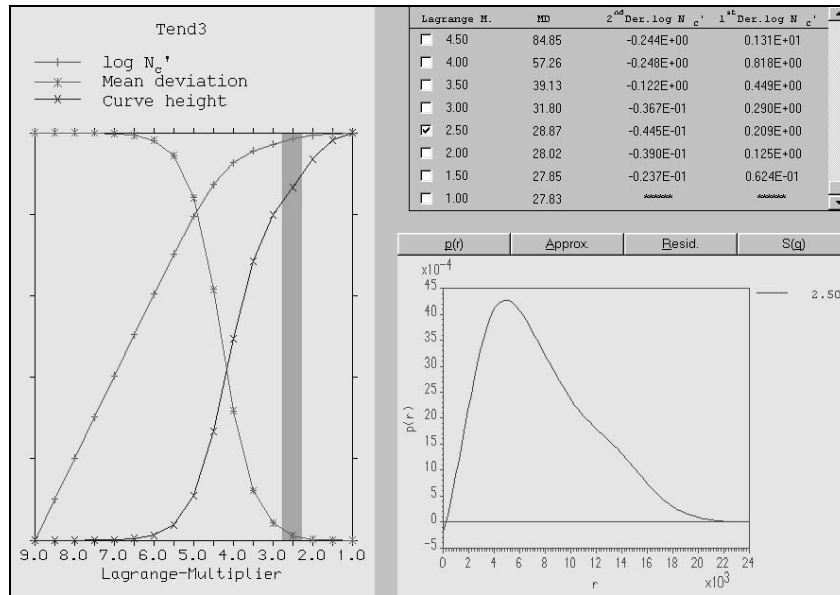


Figure 22. Screenshot from the GIFT program showing Lagrange multiplier selection. The mean deviation is near its minimum and  $\log N_c^*$  near its maximum. The resulting  $p(r)$  is displayed in the bottom right.

### 5.1.5 Validity of GIFT Results

Since there are several parameters that can be adjusted to fit the data, the issue of changing the fit to get the desired results arises. This is extremely difficult, if not impossible, to do. An extremely good fit may result in a meaningless  $p(r)$  curve, and an excellent looking  $p(r)$  may have a terrible fit to the data. For example, figure 23 shows a reasonable  $p(r)$  curve. It shows a pattern typical of elongated structures; however, the associated fit shows that the parameters used are unacceptable.

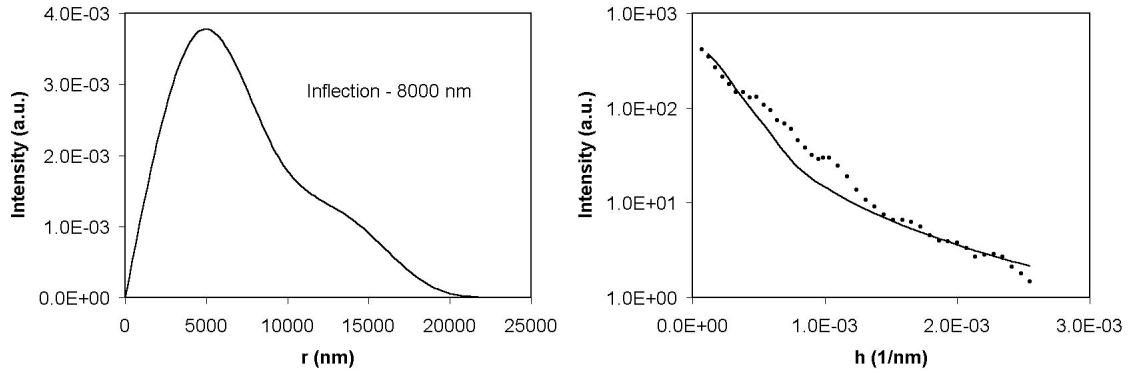


Figure 23. (left) Typical  $p(r)$  curve for elongated structures. (right) Although the  $p(r)$  curve looks acceptable, the fitting parameters provide a poor representation of the data.

## 5.2 Tissue

### 5.2.1 Type of Tissue

A primary concern of this work was acquiring sufficient samples and data so a meaningful conclusion could be drawn from data analysis. With the aid of the Department of Biomedical Engineering at WPI, fresh Achilles' tendons from rabbits were obtained from the University of Massachusetts Medical Center in Worcester. Optical microscopy and previous work on samples indicated that fiber size fell within an acceptable range for light scattering experiments. Once the tendons were harvested, they were stored for one week in phosphate buffered saline while fixatives were selected and ordered. That autolysis (self-digestion) had minimal impact on the results obtained is supported by the agreement of scattering patterns for samples (40 and 400 gram loads) that were used immediately after harvesting.

### **5.2.2 Fixation and Sectioning Options**

A wide variety of fixatives exists for use on tissue. Fixatives cross-link the collagen chains, preventing movement of collagen molecules and hence the entire tendon. The most common fixatives used collagen structures include formalin, glutaraldehyde, and Karnovsky's fixative. Formalin is able to rapidly penetrate samples, while glutaraldehyde takes longer to diffuse through. On the other hand, glutaraldehyde is a much stronger fixative than formalin. Karnovsky's fixative is a combination of formalin and glutaraldehyde. Glutaraldehyde was the chosen fixative. Since fixing time was not critical, Karnovsky's fixative was not needed. The stronger fixing effect of glutaraldehyde was desired, since the tendons would be placed under tension and could fix for any amount of time. Setting time ranged from two and a half to three hours.

In order to section the tissue after fixation, an embedding medium was required. Standard histology labs use paraffin, and there did not appear any reason to deviate from this procedure. In order to embed the tendons in paraffin, they first required dehydration. This is accomplished by soaking the tendon in increasing concentrations of alcohol. Melted paraffin (approximately 60°C) is then poured into a small rectangular box which contains the tendon. Once the paraffin has solidified, the block is placed into a microtome. Then, the tendon is sliced in sections ten microns thick. This allowed maximum transparency while minimizing damage to the structure of the fibers. All sectioning related operations (except fixation) were performed by the Histology Department at the University of Massachusetts Medical Center in Worcester.

### 5.2.3 Applying Loads to the Tendons

Rather than simply analyzing tendons under similar conditions, the tendons were placed under increasing amounts of stress. There are two reasons for doing this. First, fibers scatter perpendicular to their orientation. As more force is applied, the uncrimping of the fibers should have a visible effect on the scattering pattern as a whole. Second, to see if there was any measurable effect on fiber diameter. Tendon is designed to handle large amounts of stress in an anisotropic manner difficult to reproduce by man-made materials. Further insight and more advanced characterization techniques are steps toward such a material. The apparatus used to load the tendons is shown in figure 24 (see section 9.4.3 for fixation and loading procedure).

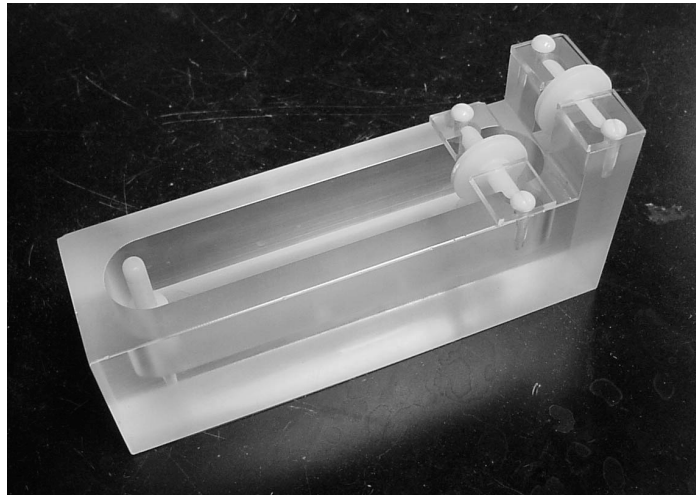


Figure 24. Apparatus used to apply loads to the rabbit tendons. Using suture material, the tendon was tied to a post (left). The suture tied to the other end of the tendon was threaded through the plastic wheels and tied to weights.

The amount of weight applied to the tendon was based on the stress-strain curve of rabbit Achilles' tendons [32] (see figure 25). The toe region is where normal physiological forces lie. The linear and yield regions were not investigated. A creep test, strain versus time, shows how a sample reacts to a constant force. Ideally, the tendons will not continue to change their length while sitting in the fixative. Figure 26 shows a creep test done on a rabbit Achilles' tendon under a stress of 0.8 MPa (5 N) for 30 minutes [32]. Tendons were placed under a load for ten minutes in a PBS bath before glutaraldehyde was added. This allowed the tendon to equilibrate with the applied load.

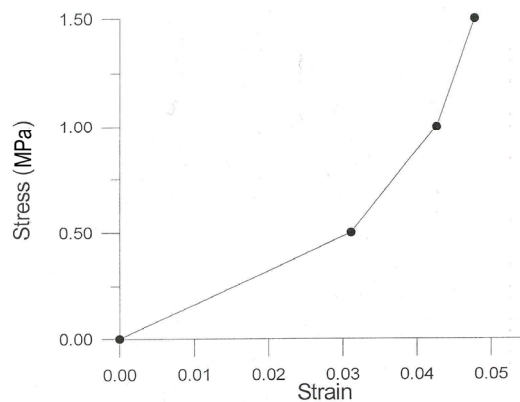


Figure 25. Stress-strain curve for rabbit Achilles' tendon [29]. The trend of the curve shows the toe region, where the uncrimping of the fibers causes non-linear behavior.

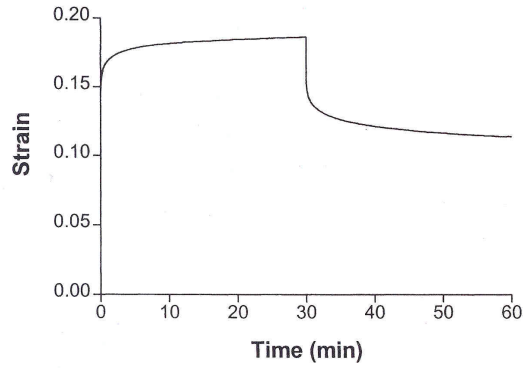


Figure 26. Creep test showing the behavior of a rabbit Achilles' tendon under a 0.8 MPa stress [29]. Based on this, tendons loaded for 10 minutes before the addition of glutaraldehyde.

### 5.3 Data Analysis and Optical Microscopy

One of the motivations of this work was the comparison of SALS analysis and optical microscopy. In all, 37 scattering patterns were analyzed from eight slides. Figure 27 shows the relative positions of all the patterns taken.

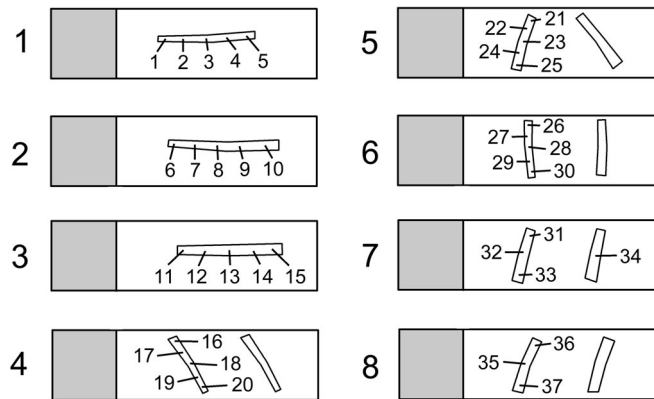


Figure 27. Eight slides were used to take 37 scattering patterns. The general area of each run is indicated.

Slides 1,2, and 3 each had a load of 40 grams applied. Slide 4 had a 100 gram load applied. Slide 5 had a 150 gram load applied. Slide 6 had a 200 gram load applied. Slides 7 and 8 had a 400 gram load applied. Slides 1,2,3,7, and 8 were part of the initial work. Slides 4,5, and 6 were used to fill in gap between loads. Attempt were made to take 5 scattering patterns from one tendon on each slide. Irregularities, possibly due to sectioning, on slides 7 and 8 made that impossible without introducing artifacts.

### 5.3.1 Determination of Average Fiber Diameter

All but one of the scattering patterns (number 17) were adequately fit using GIFT. Reasons why number 17 could not be fit are unclear, particularly since the data appears similar to other runs (see figure 28). The problem may lie in what structures were scattering, or the correct set of parameters were not found. This occurrence also may be an anomaly, given the larger amount of data that was analyzed.

No assumption was made about shape in GIFT. The assumption that the fibers were circular cylinders in GIFT produced no meaningful fit or  $p(r)$ . This is most likely due to the fibers not being sufficiently shaped like a circular cylinder. Therefore, the average fiber diameter was determined from the leftmost inflection point in the  $p(r)$  curves. Equation 27 is typically used to calculate second derivatives from data.

$$F''(x) = \frac{F(x + \Delta x) - 2 * F(x) + F(x - \Delta x)}{(\Delta x)^2} \quad (27)$$

The inflection point will be found where the second derivative changes from negative to positive. Table 2 presents the results. Graphs and corresponding fitting parameters can be found in the appendix (section 8.3).

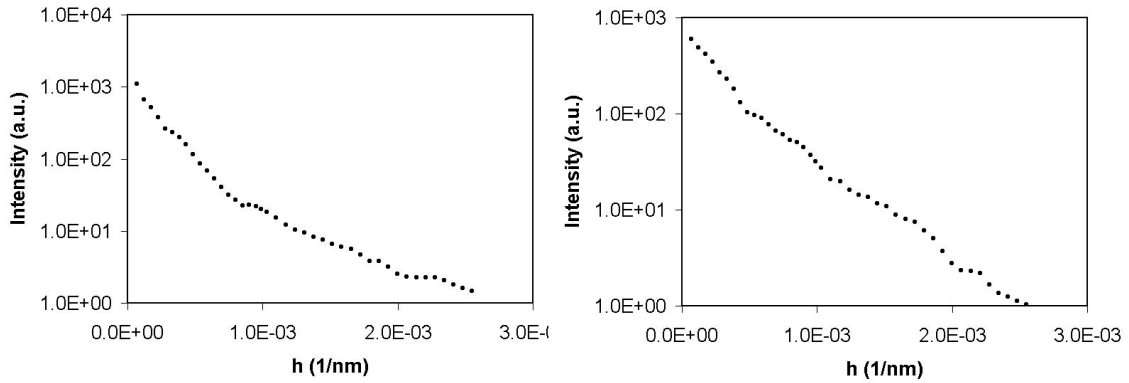


Figure 28. Raw data comparison of run 17 (right) which could not be adequately fit, with run 16 (left) which was able to be fit.

Figure 29 shows an example representative of all the analyzed data. This data is from run 14. The  $p(r)$  curve shows the structure is elongated, which is what one would expect since collagen fibers have the same characteristic. To find the average diameter from the  $p(r)$  curve, equation 27 is used to find the leftmost inflection point. In this case, the inflection point corresponds to an average diameter of 9700 nm.

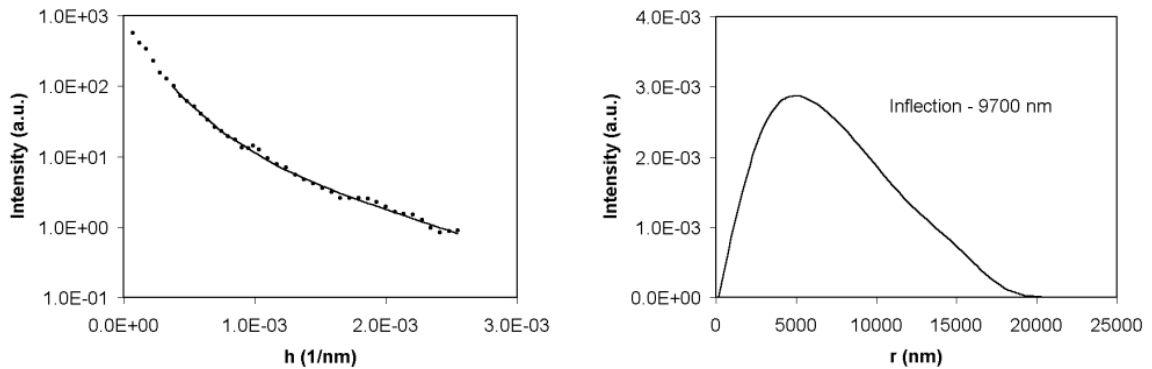


Figure 29. Example of fit for raw data (left) and the resulting  $p(r)$  curve. The  $p(r)$  curve shows an elongated structure with a cross section diameter of 9700 nm. Fitting parameters (run 14) were  $D_{max} = 24000$ ,  $NB = 8$ , and  $\lambda = 2.0$ .

The overall average fiber diameter is 8.0 microns, with a standard deviation of 2.1 microns. The results appear quite consistent with the exception of a few outliers. In particular, the analysis of run 27 produced an average fiber diameter of 3.9 microns. While 3.9 microns is still a reasonable value for the diameter of a collagen fiber, it does fall far from the average of 8.0 microns. The raw data did not show any abnormalities (see figure 58 in appendix).

Table 2. Average tendon fiber diameter calculated from p(r) curves. Average diameters occur at the leftmost inflection point.

Slide #	Run #	Average Diameter ( $\mu\text{m}$ )	Slide #	Run #	Average Diameter ( $\mu\text{m}$ )
1	1	7	5	21	6
	2	9.9		22	8.2
Stress =	3	8	Stress =	23	6.7
0.12 Mpa	4	10.5	0.45 Mpa	24	6
	5	8.2		25	5.7
2	6	7.3	6	26	7
	7	5.2		27	3.9
Stress =	8	5.4	Stress =	28	11.9
0.12 Mpa	9	8.6	0.60 Mpa	29	7.7
	10	6.6		30	9.3
3	11	7.9	7	31	6.8
	12	9.8		32	12
Stress =	13	7.2	Stress =	33	10.5
0.12 Mpa	14	9.7	1.20 Mpa	34	7.5
	15	8.2			
4	16	11	8	35	11.6
	17	-		36	11
Stress =	18	6.8	Stress =	37	7.5
0.30 Mpa	19	5	1.20 Mpa		
	20	7.2			

### 5.3.2 SALS Results versus Optical Microscopy

Stained slides were prepared from the tendons with 40 and 400 gram loads. The slides were photographed by placing a digital camera up to the eyepiece of the microscope. The eyepiece included a reference scale, where each individual mark represents one millimeter unmagnified. Figure 30 shows results from the tendon loaded with 40 grams, while figure 31 shows the tendon loaded with 400 grams. Both figures support 8 microns as a realistic average fiber diameter.

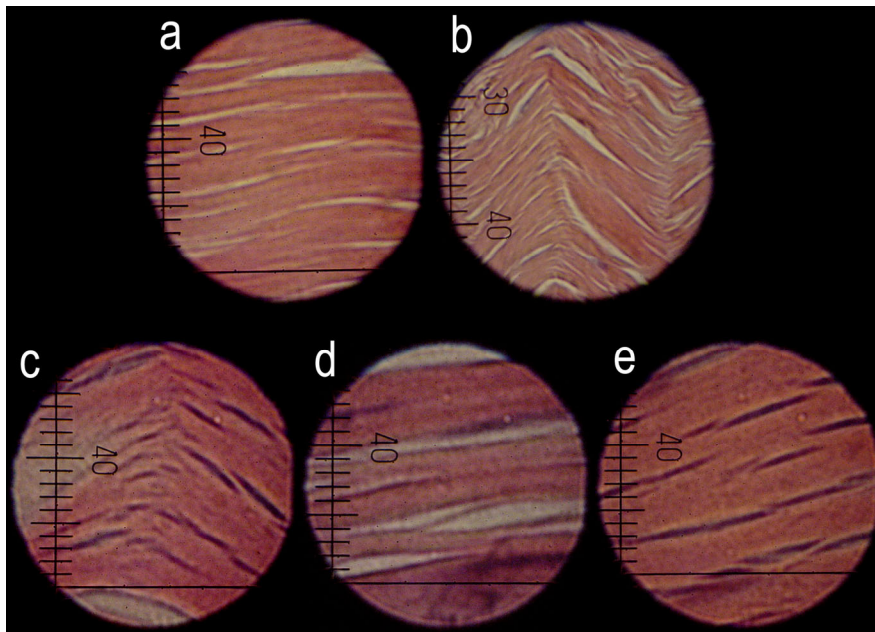


Figure 30. Stained tendon with 40 gram load applied. (a) and (b) are 200x magnification (1mm = 5 microns). (c), (d), and (e) are 400x magnification (1mm = 2.5 microns).

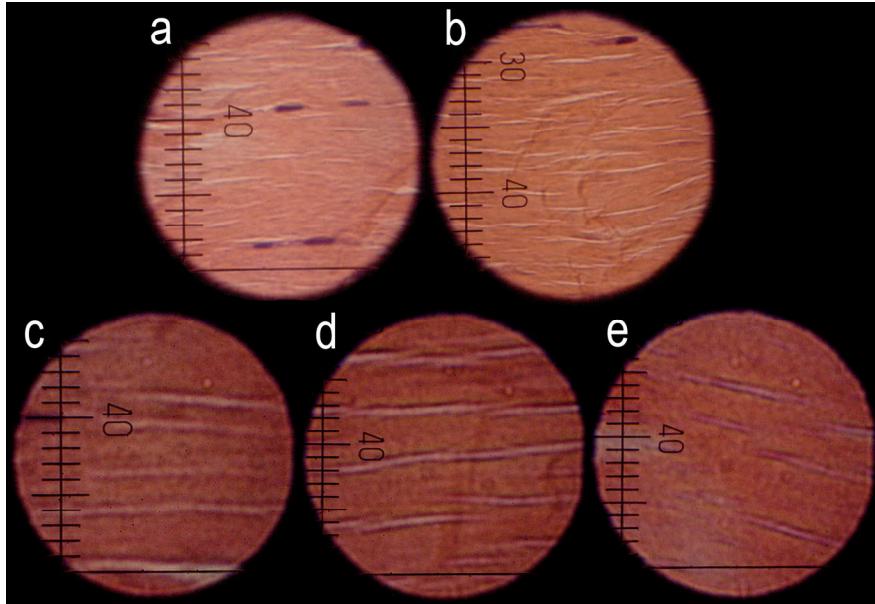


Figure 31. Stained tendon with 400 gram load applied. (a) and (b) are 200x magnification (1mm = 5 microns). (c), (d), and (e) are 400x magnification (1mm = 2.5 microns).

There are some noticeable differences between figures 30 and 31. A 40 gram load, while being sufficient to suspend the tendon in the glutaraldehyde bath, did not uncrimp the fibers. This is seen in figure 7 (b). On the other hand, no crimping could be found in the tendon with a 400 gram loading. Comparing (a) and (b) in both figures, individual fibers or clumps of fibers are seen more easily in figure 30. At higher magnifications, the fibers appear more aligned in figure 31, consistent with the higher load used.

Another feature of the tendons is the branching of fibers. Fibers do not appear to be single structures isolated from other fibers, as seen clearly in figure 30 (e). Despite the complex nature of these structures, 8 microns is still a reasonable average fiber diameter. The joining of fibers generally seems followed by another branching close by. While

these larger structures will have an effect on the scattering pattern, the overwhelming number of smaller fibers will have more of an impact on the data.

### 5.3.3 Effect of Stress on Scattering Patterns

Since fibers scatter perpendicular to their orientation, the increasing loads placed on the tendons should effect fiber alignment and scattering pattern. Smaller loads will have less effect on the crimping, while larger loads will cause uncrimping. The more the crimping is undone, the flatter and more elongated the scattering pattern should become. This is confirmed by figure 30.

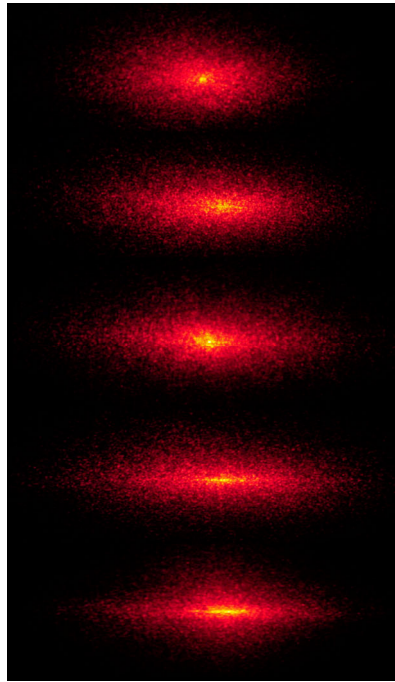


Figure 32. Photographs of the scattering created by tendons. From top to bottom, the loads applied were 40, 100, 150, 200, and 400 grams respectively.

In order to perform an orientation analysis, it is necessary to take a two dimensional scattering pattern. This requires the use of a CCD camera to measure the intensity, which our current experimental setup does not have. Adding an orientation analysis would aid in showing that the different loads applied to the tendons were having an effect on the fiber structure of the tendon. Rather than simply using optical microscopy to show the uncrimping, this phenomenon could also be related back to light scattering.

## **6. Conclusions and Recommendations: Tendons**

The most important conclusion that can be drawn from this work, is that small angle light scattering analysis is a useful technique to aid in the characterization of collagen fibers. The results compare favorably and consistently with fiber sizes seen in optical microscopy. Even though optical microscopy only allows for two dimensional observation of fibers, the results do support the three dimensional analysis provided by small angle light scattering. The drawbacks to using tendon include opacity (due in part to the paraffin embedding) and its complex fiber structure. Most of the opacity problem was avoided by melting the wax with hot air while data was being acquired. Although the paraffin can be removed by xylene, this opens up the tissue to degradation over time. Should more data need to be taken, paraffin removal is an undesirable path to take.

Surely there are more ideal tissues on which this analysis could be performed, but rabbit tendons were available in sufficient quantity to establish meaningful statistics. Tissues which could be considered easier to analyze include membranes and tissue associated with the eye, since eye related tissue must allow light to pass through. The fact that the results appear valid despite some obstacles is very promising, and attests to the robust nature of small angle scattering analysis.

Some directions for future work include further modification of the lenses used to shrink and collimate the beam and alternatives ways to mount the sample. Although our beam size was roughly 750 microns, the samples being dealt with are only slightly bigger in cross section. Shrinking the beam size further while not sacrificing collimation would be extremely worthwhile. This would make the elimination of edge effects easier to

overcome, especially if smaller samples need to be looked at. This would also open the possibility to look at local variations within a single sample. The elimination of scattering “noise” created by the glass slide on which the tendons are mounted would improve the quality of the data. The fiber diameters in the rabbit tendons were small enough that data at very small angles was not compulsory. In order to examine fibers of larger diameter, which scatter at smaller angles, this improvement would become a necessity since the intensity of background scattering (the slide) increases substantially at small angles.

Finally, the amount of load placed upon the tendons should be extended into the linear region and if possible the yield region. Although we did not investigate this area because normal physiological forces are not that high, it would nonetheless be interesting to examine the effects of higher loads. This could offer insight into tendon damage in injuries. Higher stress may also require a different method of securing the tendon, as the sutures may slip off. Stress-strains curve beyond the toe region of rabbit Achilles tendon were not found in literature. Therefore, experimentation in this area is also recommended.

## **7. Articular Cartilage**

### **7.1 Purpose and Structure**

Articular cartilage provides a low friction surface for the motion of load bearing joints, and is composed of collagen (type II, 50-73% dry weight), proteoglycan (15-30% dry weight), and water (58-78% wet weight) [33]. Unlike tendon, articular cartilage bears significant load in three dimensions; therefore, the structure will differ significantly from tendon despite common structural components (fibrils, proteoglycan, etc.). The following general discussion is adapted from *Biomechanics of Diarthrodial Joints* [34].

Figures 33 and 34 show the structure and regions of articular cartilage. Starting on the articular surface and working toward the bone, the superficial tangential zone is found first. This zone contains collagen fibrils mainly oriented parallel to the articulating surface. These fibers are characterized by a smaller diameter and denser packing than the rest of the cartilage. Chondrocytes (cells) are oval shaped and also oriented parallel to the articulating surface. The middle zone contains fibrils that are more randomly arranged and have a larger diameter than fibrils in the superficial tangential zone. Chondrocytes in this region are also more circular in shape. The deep zone contains radially oriented fibrils and chondrocytes. The chondrocytes form column like structures. The calcified zone is what binds the cartilage to the bone beneath.

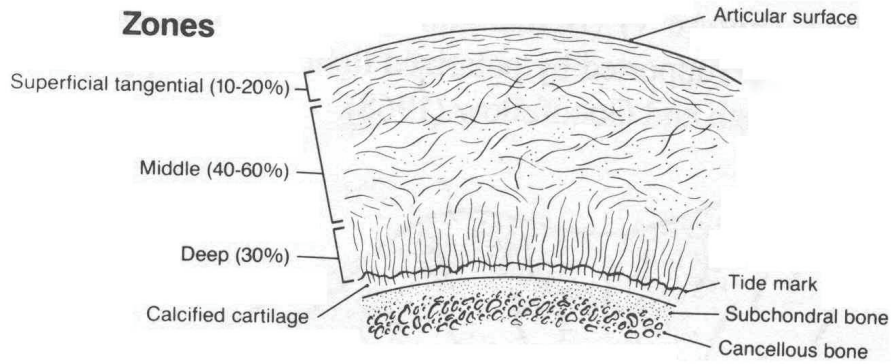


Figure 33. Diagram displaying the various regions of articular cartilage and the general orientation of collagen fibrils within each region [34].

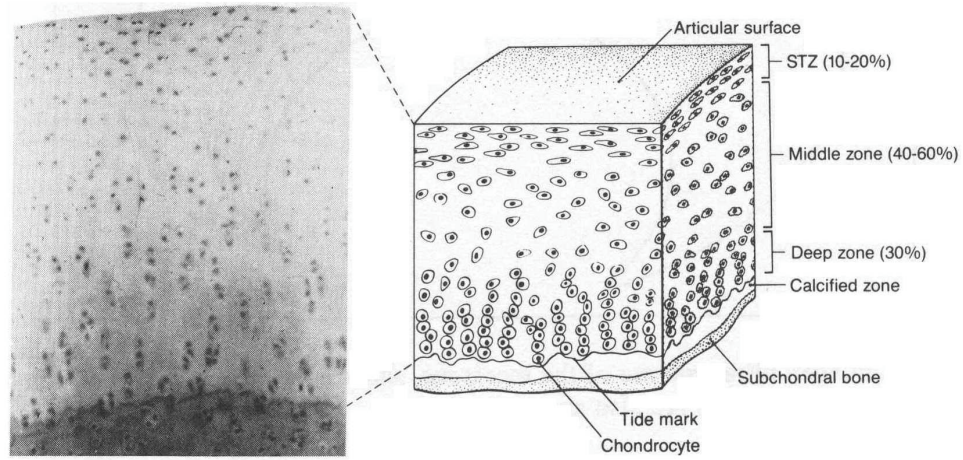


Figure 34. Micrograph and diagram depicting the shape and distribution of chondrocytes within articular cartilage [34].

## 7.2 Small Angle Scattering Comparison of Healthy and Osteoarthritic Human Articular Cartilage

Human articular cartilage samples (osteoarthritic and normal) samples were obtained from the Department of Orthopedics at Brigham and Women's Hospital (Boston, MA). The samples were embedded in paraffin and sectioned at a thickness of 10 microns. Figures 35, 36, and 37 show the raw data (with background scattering subtracted) of articular cartilage samples.

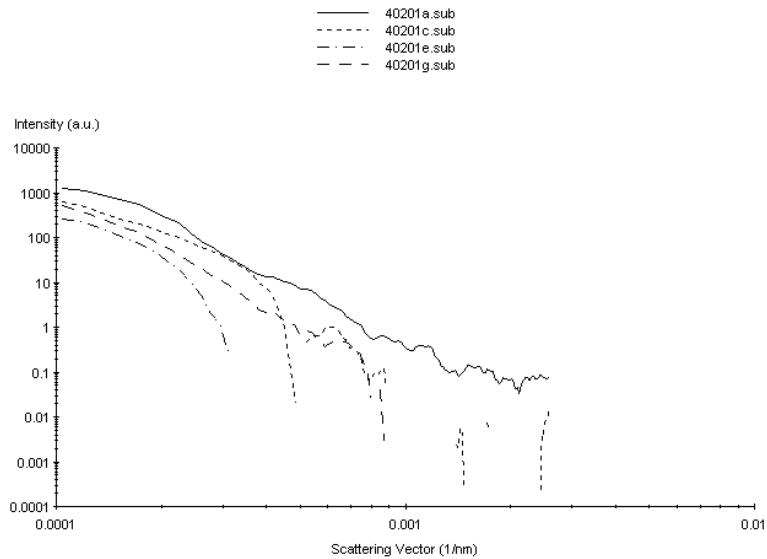


Figure 35. Scattering at various azimuthal angles from a section of osteoarthritic articular cartilage where very little collagen is present. (a) articular surface parallel to plane of detection. (b) rotated 30°. (c) rotated 60°. (d) rotated 90°.

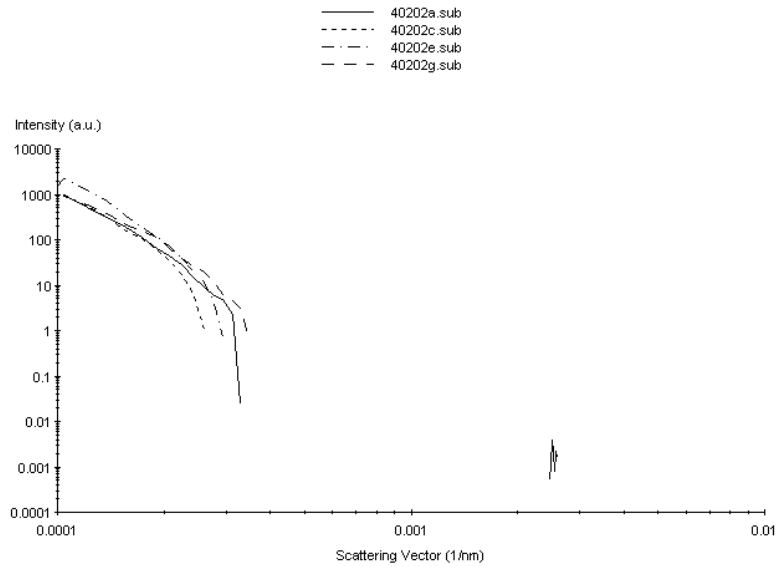


Figure 36. Scattering at various azimuthal angles from a section of osteoarthritic articular cartilage where collagen is present. (a) articular surface parallel to plane of detection. (c) rotated 30°. (e) rotated 60°. (g) rotated 90°.

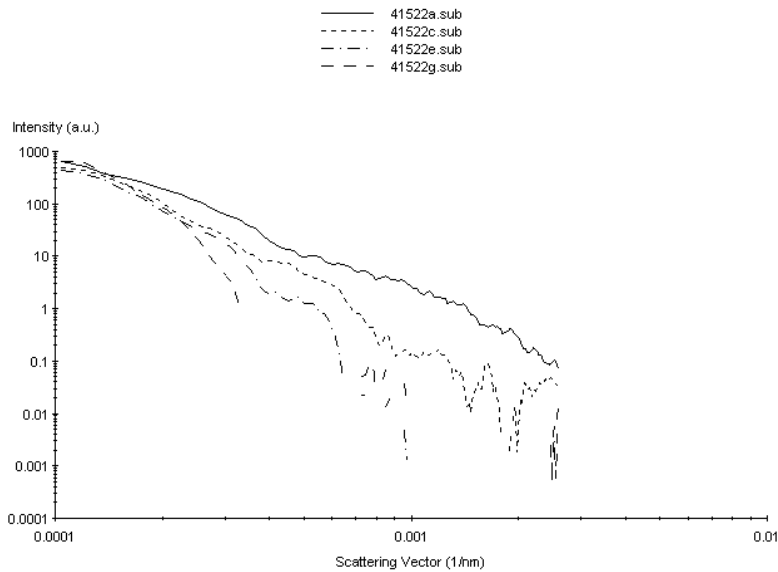


Figure 37. Scattering at various azimuthal angles from a section of articular cartilage. (a) articular surface parallel to plane of detection. (c) rotated 30°. (e) rotated 60°. (g) rotated 90°.

Figure 35 is a scattering pattern measured on a section of osteoarthritic cartilage where collagen is scarce (as seen in polarized light microscopy). There are orientation effects when comparing the various azimuthal angles. When the articulating surface is parallel with the plane of detection, intensity is higher over the whole range of detection. This indicates elongated structures perpendicular to the articulating surface. Figure 36 (obtained from a different spot on the same sample) shows a significant difference in scattering. The intensity drops off more sharply as the scattering vector increases. This is indicative of larger structures scattering, since there is an inverse relationship between particle size and scattering angles. Polarized light microscopy revealed the presence of degraded collagen.

Figure 37 differs from both figures 35 and 36. There is a noticeable orientation effect, with intensity falling off more rapidly as the sample is rotated. The most likely explanation for the change in scattering as a function of azimuthal angle are the structures formed by the chondrocytes and their spacing. These structures, particularly in the deep zone, form column like structures perpendicular to the articulating surface.

Comparing the three scattering patterns, each shows a distinct trait. Figures 35 and 37, while similar, differ in the small scattering vector region. There is a significant difference in the intensities at the minimum scattering vector for each azimuthal angle in figure 35, while all the scattering plots in figure 37 appear to converge. The scattering intensities in figure 36 all fall into the background scattering pattern at a scattering vector around  $0.0003 \text{ nm}^{-1}$ , which is not seen in either of the other scattering patterns. There are two structures responsible for the differences in these scattering patterns, collagen and the

chondrocytes. Further work is needed to determine if these differences can be related to collagen content, chondrocyte structures, or arthritic degradation.

## 8. References

- [1] Guinier, A. and Fournet, G. *Small Angle Scattering of X-Rays*. Wiley, New York, 1955.
- [2] van de Hulst, H.C. *Light Scattering by Small Particles*. Wiley, New York, 1957.
- [3] Kerker, M. *The Scattering of Light and Other Electromagnetic Radiation*. Academic Press, New York, 1969.
- [4] Glatter, O. and Kratky, O. *Small Angle X-Ray Scattering*. Academic Press, New York, 1982.
- [5] Bohren, C.F. and Huffman, D.R. *Absorption and Scattering of Light by Small Particles*. Wiley, New York, 1983.
- [6] Debye, P. *Ann. Physik* **46**, 809.
- [7] Porod, G. *Acta Phys. Austriaca* **2**, p. 255-292.
- [8] Pedersen, J. *Adv. Colloid and Int. Sci.* **70**, p. 171-210
- [9] Glatter, O. *Acta Physica Austriaca.* **47**. p. 83-102.
- [10] Greville, T.N.E. *Theory and Applications of Spline Functions*. Academic Press, New York, 1969.
- [11] Schelten, J. and Hossfeld, F. *J. Appl. Cryst.* **3**, p. 137-145.
- [12] de Boor, C. *A Practical Guide to Splines*. Springer-Verlag, New York, 1978.
- [13] Glatter, O. *J. Appl. Cryst.* **10**, p. 415-421.
- [14] Bracewell, R.N. *Fourier Transform and its Applications*. McGraw-Hill, New York, 1965.
- [15] Damaschun, G. and Schmidt, P.W. *Acta Cryst.* **A27**, p. 193-197.
- [16] Damaschun, G. and Schmidt, P.W. *Monatsh. Chem.* **102**, p. 1146-1155.
- [17] Glatter, O. *J. Appl. Cryst.* **13**, p. 577-584.
- [18] Nimni, Marcel E. *Collagen*. Volume 1. CRC Press, Boca Raton, 1988.
- [19] Petruska, J.A. and Hodge, A.J. *Proc. Natl. Acad. Sci. U.S.A.* **51**, 1964.
- [20] Smith, J.W. *Nature (London)* **219**, 1968.
- [21] Sasaki, N. and Odajima, S. *J. Biomechanics.* **29**, 1996.
- [22] Christiansen, D. L., Huang, E.K., Silver, F.H. *Matrix Biology.* **19**, 2000.
- [23] Sacks, M.S., Smith, D.B., Hiester, E.D. *Ann. Biomedical Eng.* **25**, 1997.
- [24] Sacks, M.S., Gloeckner, D.C. *J. Biomed. Mat. R.* **46**, 1999.
- [25] Gloeckner, D.C., Sacks, M.S., Billiar, K.L., Bachrach, N. *J. Biomed. Mat. R.* **52**, 2000.
- [26] Ferdman, A.G. and Yannas, I.V. *J. Invest. Dermatol.* **100**, 1993.
- [27] CASI User's Reference Manual 085-929-101.
- [28] Schnablegger, H. and Glatter, O. *J. Coll. Int. Sci.* **158**, p. 228-242.
- [29] Brunner-Popela, J. and Glatter, O. *J. Appl. Cryst.* **30**, p. 431-442.
- [30] Weyerich, B., Brunner-Popela, J., and Glatter, O. *J. Appl. Cryst.* **32**, p. 197-209.
- [31] Cosimini, J., Vadurro, V., and Viveiros, M. Major Qualifying Project, Worcester Polytechnic Institute, 2001.
- [32] Han, S. *et al. J. Magnetic Resonance.* **144**, p. 217-227.
- [33] Sah, R.L. in *Introduction to Bioengineering*, ed. Fung, Y.C. World Scientific, New Jersey, 2001.

- [34] Mow, V.C., Hou, J.S., and Ratcliffe, A. in *Biomechanics of Diarthrodial Joints vol. 1*, eds. Mow, V.C., Ratcliffe, A., and Woo, S. L-Y. Springer-Verlag, New York, 1990.

## 9. Appendix

### 9.1 Cubic B-Spline Program

The following code was used to create the splines in figures 5 and 7. It was written in Visual Basic, and draws upon algorithms from de Boor [12].

```
Option Base 1
Dim splmat(1000, 30) As Double
Dim k, n, i, j, bspl, mflag, jderiv, counter, counter3, numpts, nb, dmax As Integer
Dim T(5), x, step, knotstep, knot(30), counter2, bc(26), bcoef As Double
```

---

```
Public Sub Command1_Click()
```

```
' Open output file for spline data
Open "c:\data\spl.txt" For Output As #1
```

```
' step - real space increment
' dmax - maximum dimension entered in GIFT program
' nb - number of splines used in GIFT
' k - spline order + 1
```

```
step = 0.05
dmax = 13
nb = 15
n = 1
k = 4
numpts = 0
```

```
Picture1.Scale (-3, 2000)-(dmax + 1, -0.0003)
Picture1.Line (0, 0)-(0, 1.5)
Picture1.Line (dmax, 0)-(dmax, 1.5)
Picture1.Line (dmax / nb, 0)-(dmax / nb, 1.5)
```

```
jderiv = 0
```

```
' spline coefficients taken from *.IO$
```

```
bc(1) = -2315.3
bc(2) = 117.98
bc(3) = 510.72
bc(4) = 2035
bc(5) = 1610
bc(6) = 1161.2
bc(7) = 1022.2
bc(8) = 815.54
bc(9) = 684.04
bc(10) = 515.85
bc(11) = 387.47
bc(12) = 252.22
bc(13) = 156.68
bc(14) = 68.696
bc(15) = 40.29
```

```

' create knot points for the splines
For counter = 1 To (nb + 4)
    knot(counter) = (Cdbl(dmax) / Cdbl(nb)) * Cdbl(counter - 4)
Next

Picture1.DrawWidth = 2

' splmat - array of spline data
' create values where splines will be evaluated
For x = -3 To dmax Step step
    numpts = numpts + 1
    splmat(numpts, 1) = x
Next

' calculate splines
' subroutines bvalue and interv are from de Boor
For counter = 1 To (nb)

    counter3 = 1
    bcoef = bc(counter)
    T(1) = knot(counter)
    T(2) = knot(counter + 1)
    T(3) = knot(counter + 2)
    T(4) = knot(counter + 3)
    T(5) = knot(counter + 4)

    For x = -3 To dmax Step step
        Call Interv
        Call bvalue
        Picture1.PSet (x, bspl)
        splmat(counter3, counter + 1) = bspl
        counter3 = counter3 + 1
    Next

Next

For counter = 1 To numpts
    For counter3 = 1 To (nb + 1)
        Print #1, Format(splmat(counter, counter3), "0.0000E+00");
        If counter3 = (nb + 1) Then
            Print #1, Chr(vbKeyReturn);
            Exit For
        End If
        Print #1, ",";
    Next
Next

End Sub

```

---

```

Public Sub bvalue()

Dim kmax, ilo, imk, j, jc, jcmn, jcmx, nmi As Integer
Dim jj, kmj, km1 As Integer
Dim aj(20), dl(20), dr(20), fkmj As Double

bspl = 0
If (jderiv >= k) Then
    GoTo label_99
End If
Call Interv
If (mflag <> 0) Then
    GoTo label_99
End If
km1 = k - 1
If (km1 > 0) Then
    GoTo label_1
End If
bspl = bcoef
GoTo label_99

label_1:
jcmn = 1
imk = i - k
If (imk >= 0) Then
    GoTo label_8
End If
jcmn = 1 - imk

For j = 1 To i Step 1
    dl(j) = x - T(i + 1 - j)
Next
For j = i To km1 Step 1
    aj(k - j) = 0
    dl(j) = dl(i)
Next

GoTo label_10

label_8:
For j = 1 To km1 Step 1
    dl(j) = x - T(i + 1 - j)
Next

label_10:
jcmx = k
nmi = n - i

If (nmi >= 0) Then
    GoTo label_18
End If

```

```

jcmx = k + nmi
For j = 1 To jcmx Step 1
  dr(j) = T(i + j) - x
Next
For j = jcmx To km1 Step 1
  aj(j + 1) = 0
  dr(j) = dr(jcmx)
Next

GoTo label_20

label_18:
For j = 1 To km1 Step 1
  dr(j) = T(i + j) - x
Next

label_20:
For jc = jcmx To jcmx Step 1
  aj(jc) = bcoef
Next

If (jderiv = 0) Then
  GoTo label_30
End If

For j = 1 To jderiv Step 1
  kmj = k - j
  fkmj = kmj
  ilo = kmj
  For jj = 1 To kmj Step 1
    aj(jj) = ((aj(jj + 1) - aj(jj)) / (dl(ilo) + dr(jj))) * fkmj
    ilo = ilo - 1
  Next
Next

label_30:
If (jderiv = km1) Then
  GoTo label_39
End If
For j = jderiv + 1 To km1 Step 1
  kmj = k - j
  ilo = kmj
  For jj = 1 To kmj Step 1
    aj(jj) = (aj(jj + 1) * dl(ilo) + aj(jj) * dr(jj)) / (dl(ilo) + dr(jj))
    ilo = ilo - 1
  Next
Next

label_39:
bspl = aj(1)

label_99:

```

Exit Sub

End Sub

---

Public Sub Interv()

If (x < T(1)) Then

    i = 1

    mflag = -1

    Exit Sub

End If

If (x >= T(5)) Then

    mflag = 1

    i = 5

    Exit Sub

End If

For j = 1 To (n + k) Step 1

    If (T(j) <= x) And (T(j + 1) > x) Then

        i = j

        mflag = 0

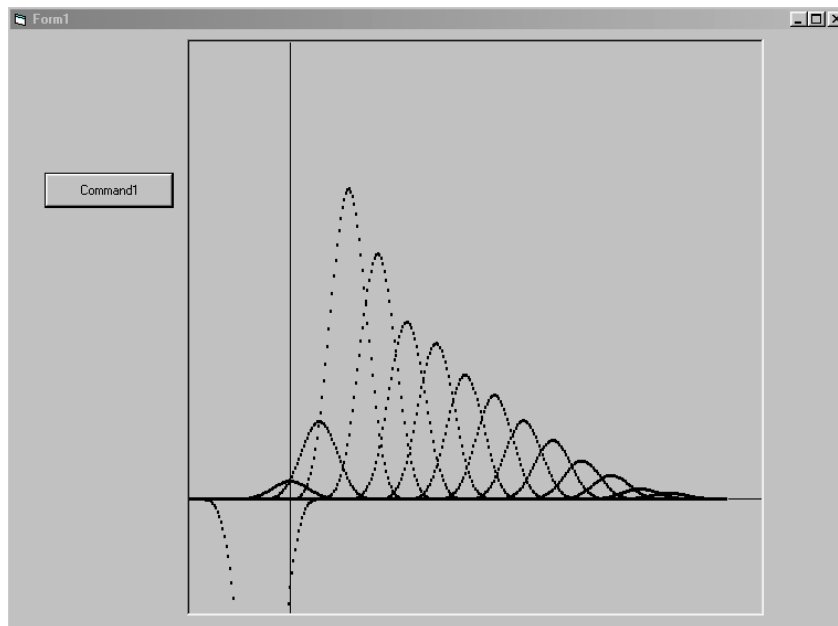
        Exit For

    End If

Next

End Sub

Screenshot:



## 9.2 Data Formatting Program

The following code was used to transform the CASI formatted data to the format required by GIFT. It was written in Visual Basic.

```
Private Sub Convert_Click()

Dim Header As String
Dim I, Counter, NegPoints, Points, HeadPts As Integer
Dim Data(2) As Double

'Number of header lines in a CASI file
HeadPts = 22

For I = 0 To (File1.ListCount - 1)

    If File1.Selected(i) Then
        Points = 0
        NegPoints = 0

        OpenFile.Text = Dir1.Path & "\ " & File1.List(i)
        OutFile.Text = Dir2.Path & "\ " & File1.List(i)

        'Count number of data points
        Open OpenFile.Text For Input As #1

        Do Until (EOF(1) = True)
            Input #1, Header
            Points = Points + 1
        Loop

        Close

        'Count number of negative points
        Open OpenFile.Text For Input As #1

        For Counter = 0 To (HeadPts - 1)
            Line Input #1, Header
        Next Counter

        Do Until (EOF(1) = True)
            Input #1, Data(0), Data(1)
            If Data(0) < 0 Then
                NegPoints = NegPoints + 1
            End If
        Loop
        Close 1

        Points = Points - HeadPts - NegPoints - 2

        Open OpenFile.Text For Input As #1
```

```

Open OutFile.Text For Output As #2

'Read header info
For Counter = 0 To (HeadPts - 1)
Line Input #1, Header
Next Counter
'Read negative points
For Counter = 0 To (NegPoints - 1)
Line Input #1, Header
Next Counter

'Write Glatter header
Print #2, ""
Print #2, ""
Write #2, Spc(5);
Print #2, Points;
Print #2, "    0    0    0    0    0    0    0"
Print #2, "0.000000E+00 0.000000E+00 0.000000E+00 1.000000E+00 0.000000E+00"
Print #2, "1.000000E+00 1.000000E+00 1.000000E+00 0.000000E+00 0.000000E+00"

'Read data, write data to output file
Do Until (EOF(1) = True)

Input #1, Data(0), Data(1)
Data(0) = Abs((4 * 3.1415 / 632.8) * Sin(Data(0) * 3.1415 / 360))
Data(2) = 0.01 * Data(1)
Text3.Text = Format(Data(0), "0.000000E+00")
Text4.Text = Format(Data(1), "0.000000E+00")
Text5.Text = Format(Data(2), "0.000000E+00")

Print #2, " ";
Print #2, Text3.Text;
Print #2, " ";
Print #2, Text4.Text;
Print #2, " ";
Print #2, Text5.Text

Loop
Close
End If

Next I
End Sub

Private Sub Dir1_Change()
File1.Path = Dir1.Path
End Sub

Private Sub Drive1_Change()
Dir1.Path = Drive1.Drive
End Sub

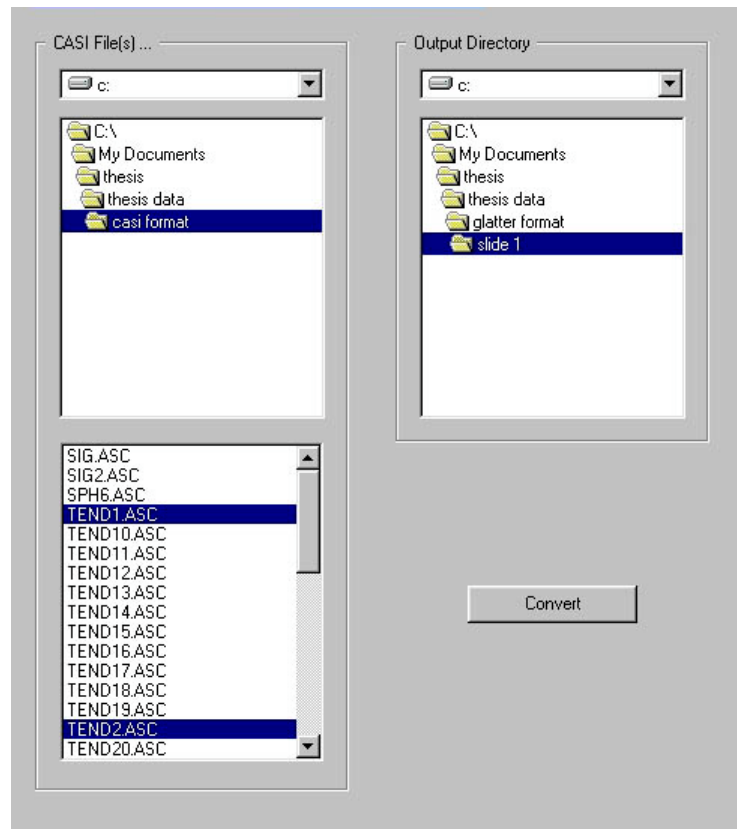
```

```
Private Sub Drive2_Change()  
Dir2.Path = Drive2.Drive  
End Sub
```

```
Private Sub Text2_Change()
```

```
End Sub
```

Screenshot:



### 9.3 Experimental Data and GIFT Results

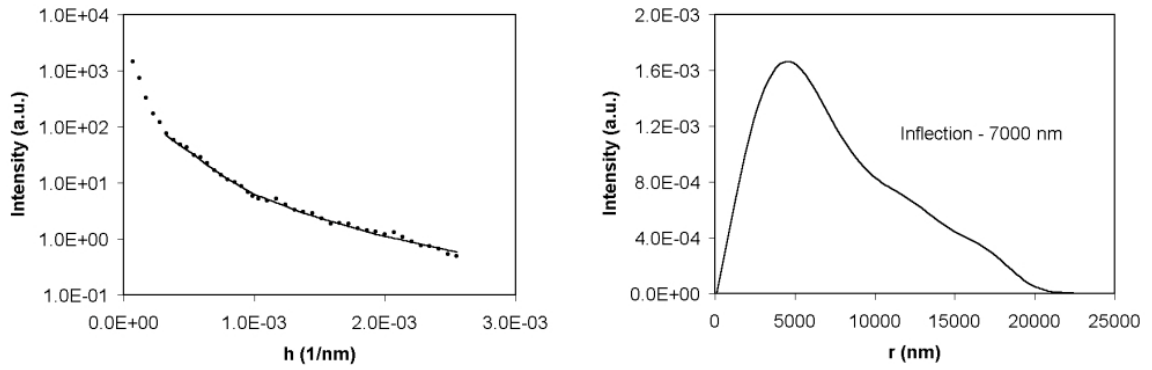


Figure 38. Run 1.  $D_{max} = 24500$ .  $NB = 10$ .  $\lambda = 3.5$ .

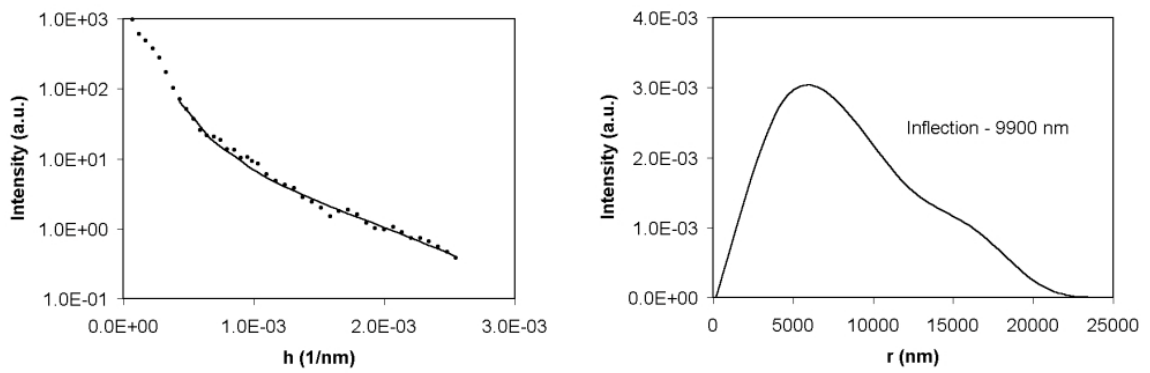


Figure 39. Run 2.  $D_{max} = 24500$ .  $NB = 6$ .  $\lambda = 2.5$ .

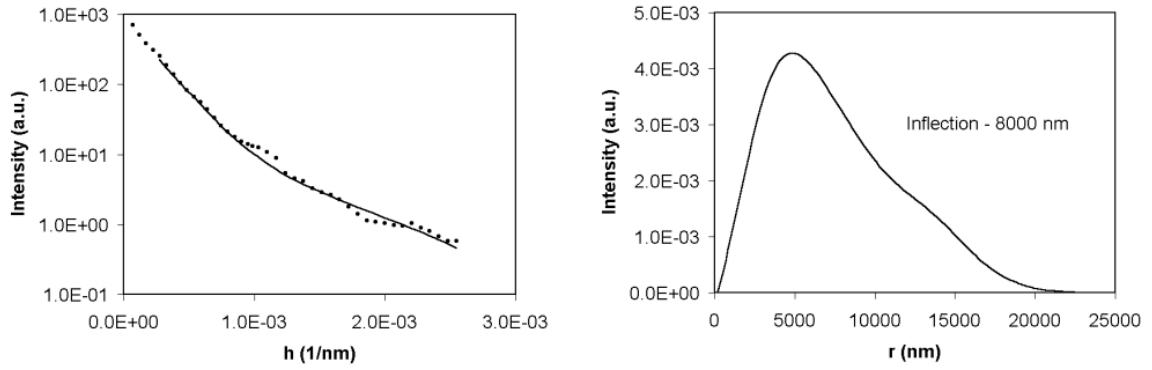


Figure 40. Run 3.  $D_{\max} = 24000$ .  $NB = 7$ .  $\lambda = 2.5$ .

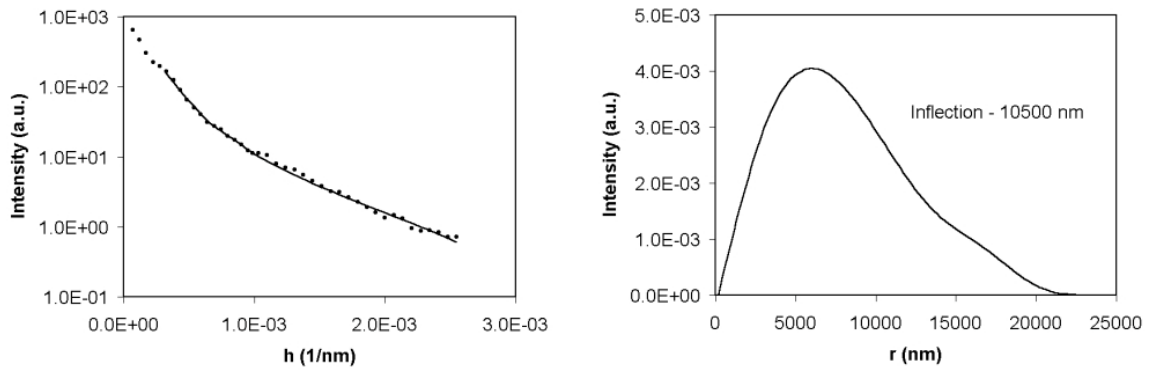


Figure 41. Run 4.  $D_{\max} = 23500$ .  $NB = 7$ .  $\lambda = 2.5$ .

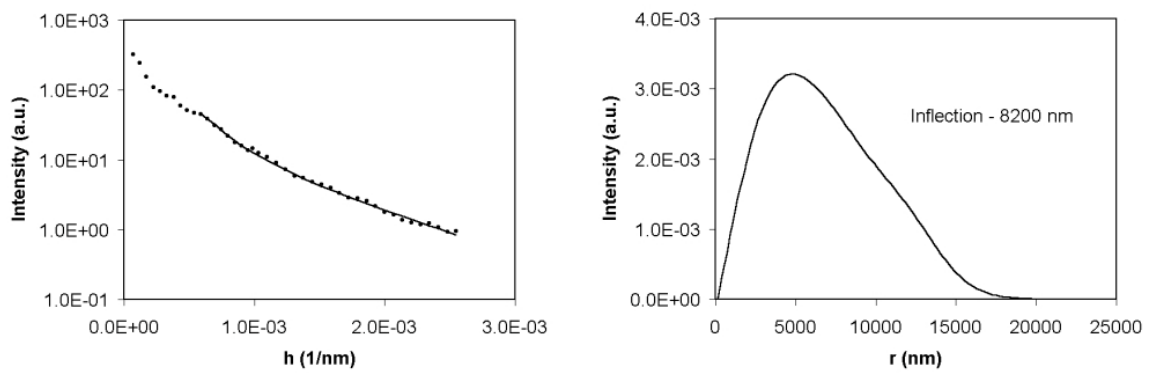


Figure 42. Run 5.  $D_{\max} = 21300$ .  $NB = 7$ .  $\lambda = 2.0$ .

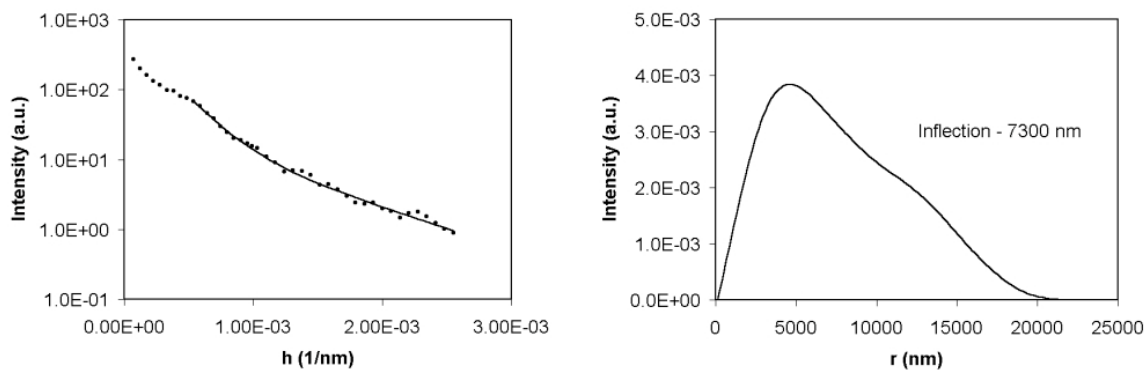


Figure 43. Run 6.  $D_{max} = 22500$ .  $NB = 7$ .  $\lambda = 3.0$ .

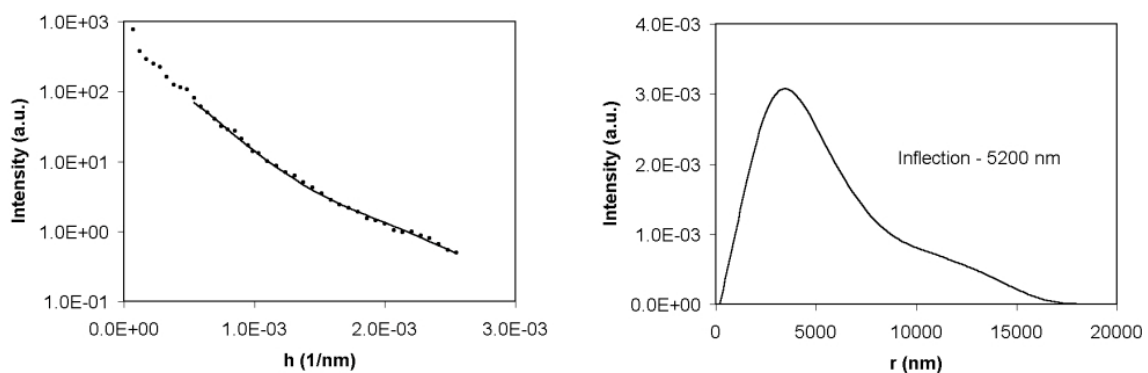


Figure 44. Run 7.  $D_{max} = 19000$ .  $NB = 7$ .  $\lambda = 2.5$ .

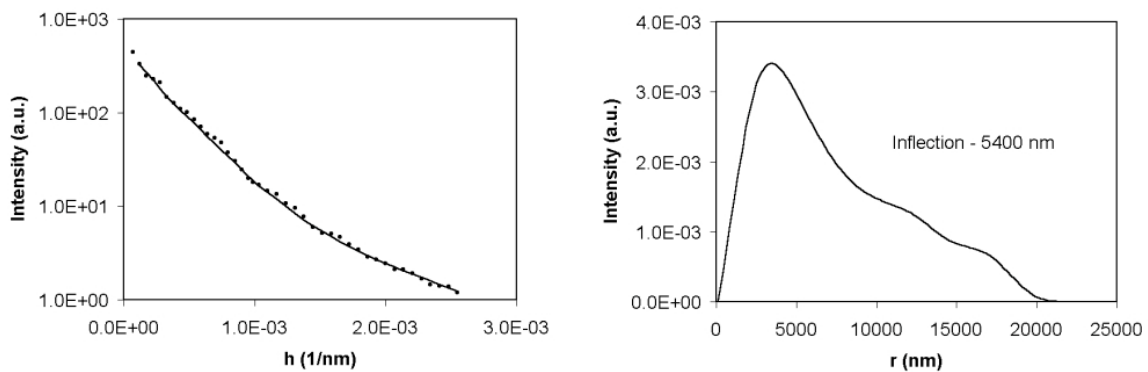


Figure 45. Run 8.  $D_{max} = 22000$ .  $NB = 9$ .  $\lambda = 4.0$ .

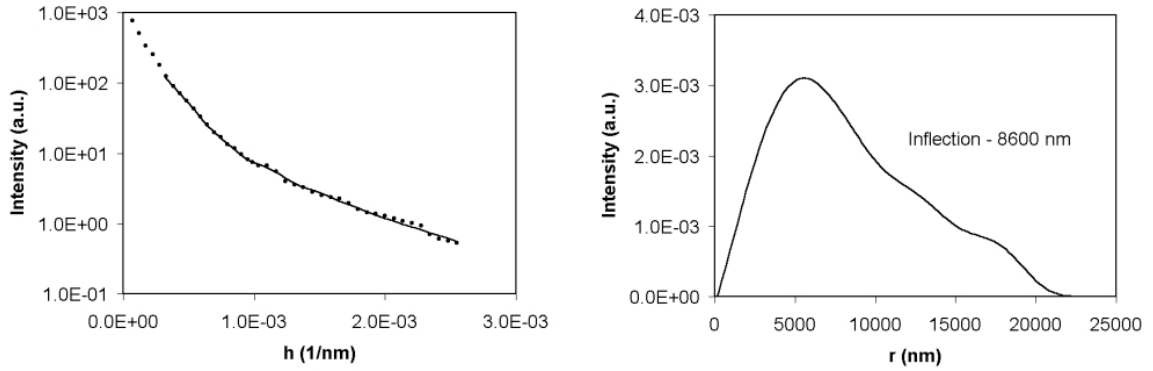


Figure 46. Run 9.  $D_{max} = 23000$ .  $NB = 9$ .  $\lambda = 2.5$ .

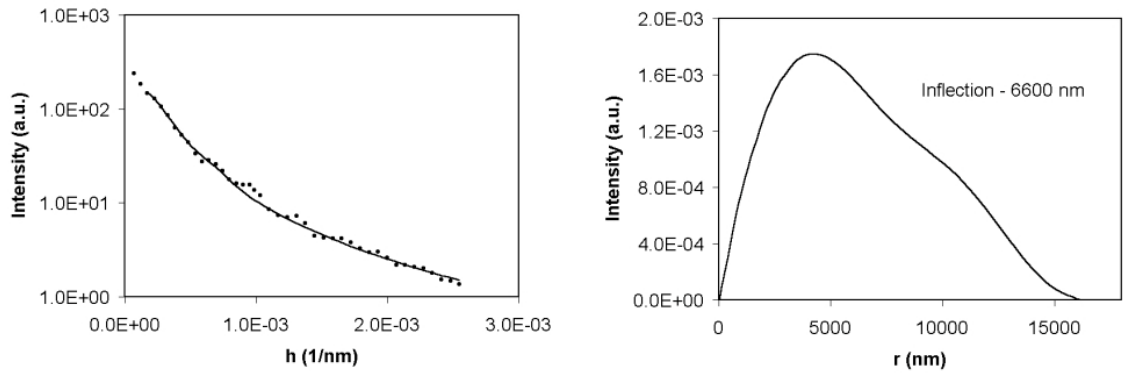


Figure 47. Run 10.  $D_{max} = 26000$ .  $NB = 7$ .  $\lambda = 3.5$ .

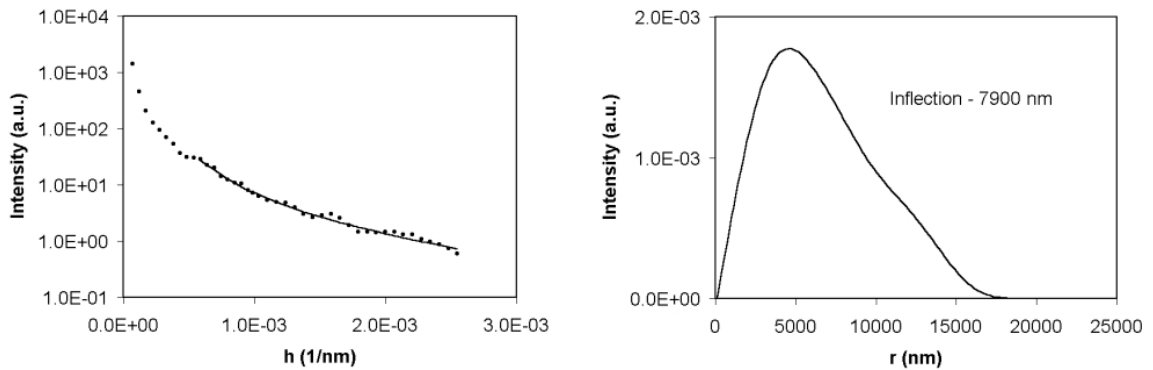


Figure 48. Run 11.  $D_{max} = 19000$ .  $NB = 6$ .  $\lambda = 2.5$ .

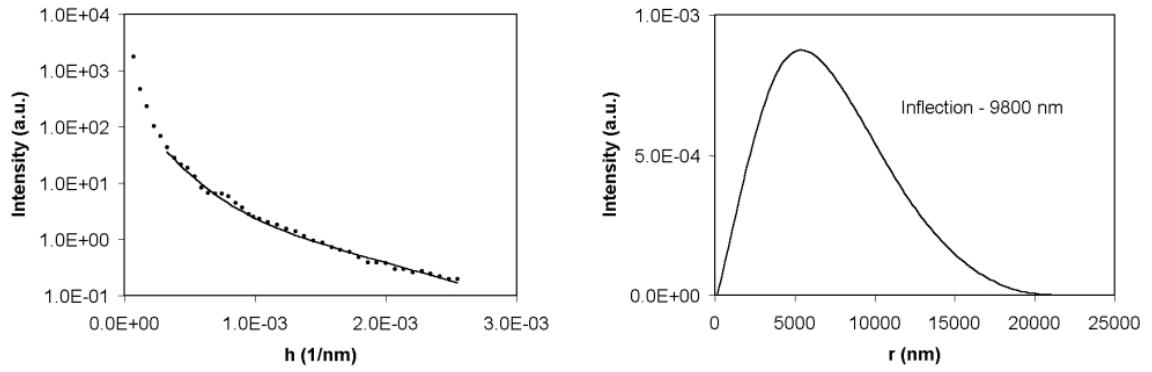


Figure 49. Run 12.  $D_{max} = 22500$ .  $NB = 6$ .  $\lambda = 3.0$ .

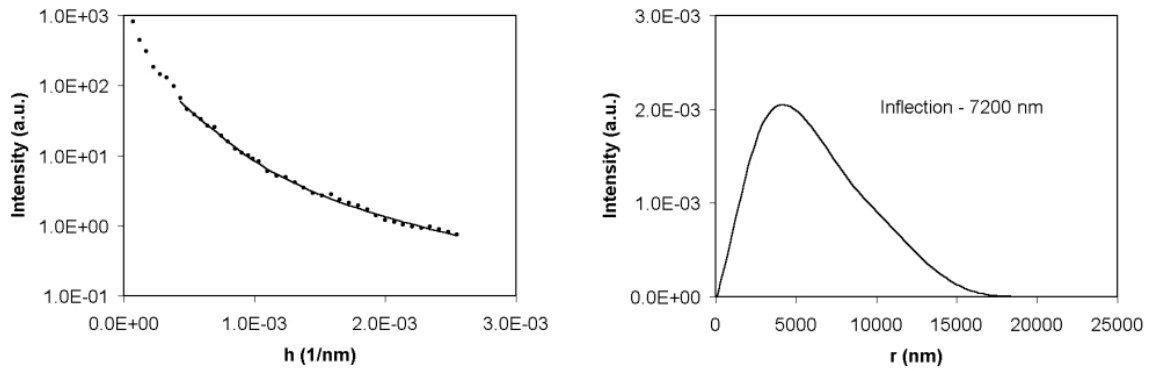


Figure 50. Run 13.  $D_{max} = 21500$ .  $NB = 8$ .  $\lambda = 2.5$ .

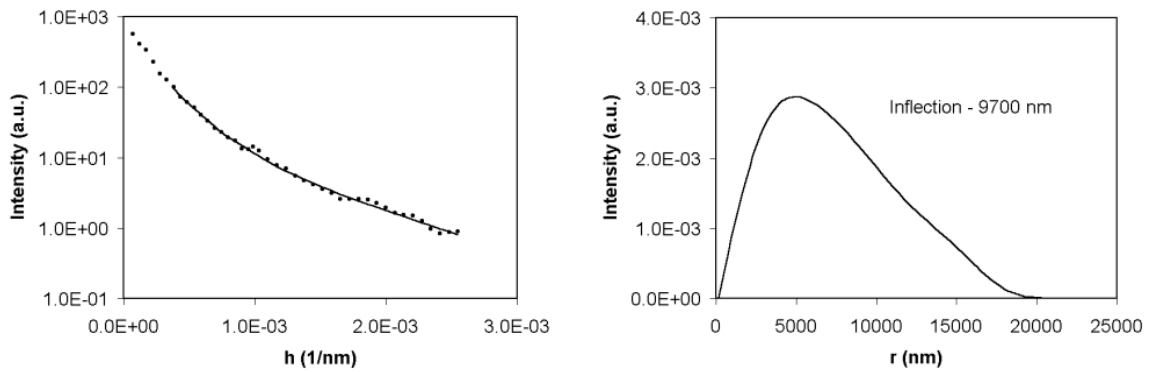


Figure 51. Run 14.  $D_{max} = 24000$ .  $NB = 8$ .  $\lambda = 2.0$ .

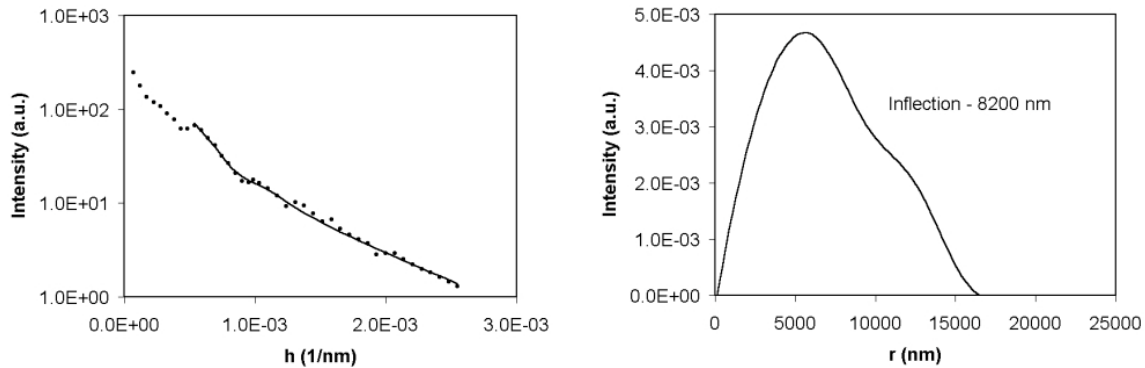


Figure 52. Run 15.  $D_{max} = 22000$ .  $NB = 7$ .  $\lambda = 3.0$ .

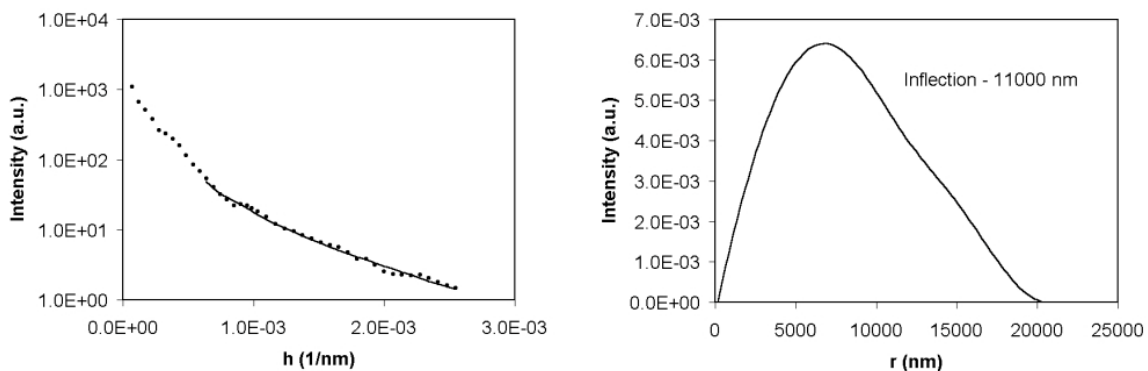


Figure 53. Run 16.  $D_{max} = 27000$ .  $NB = 7$ .  $\lambda = 2.0$ .

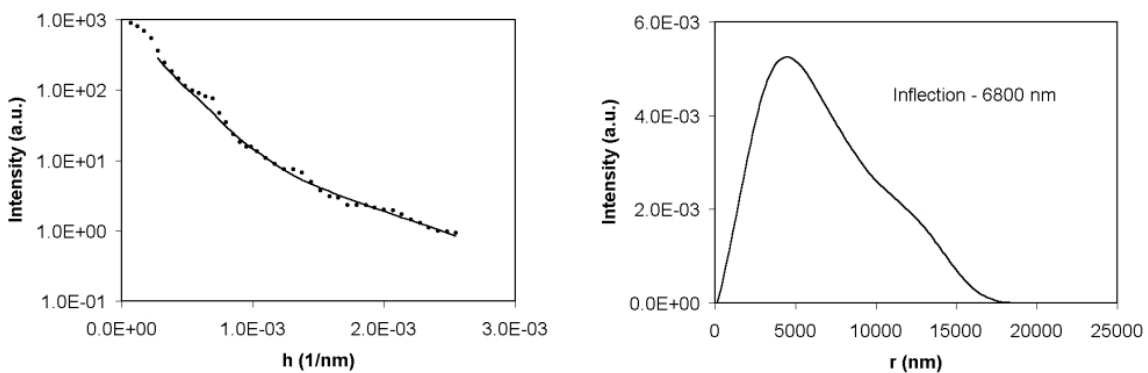


Figure 54. Run 18.  $D_{max} = 22500$ .  $NB = 7$ .  $\lambda = 2.5$ .

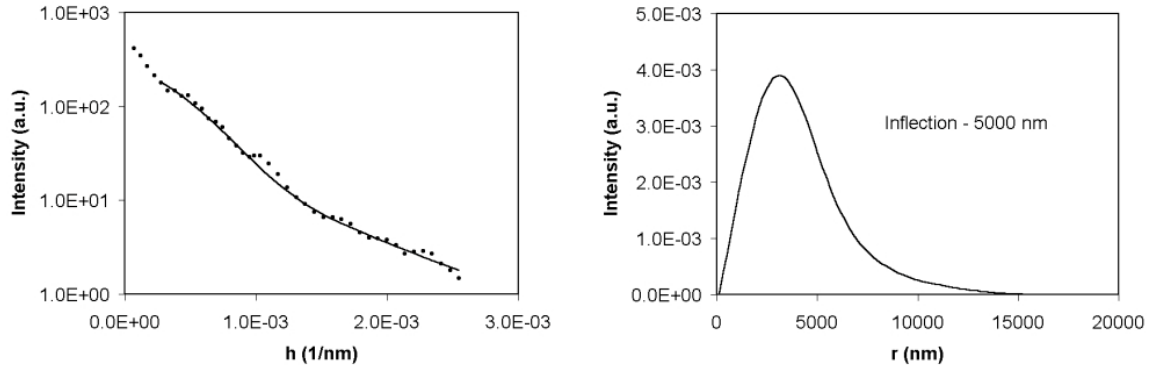


Figure 55. Run 19.  $D_{max} = 17000$ .  $NB = 6$ .  $\lambda = 3.5$ .

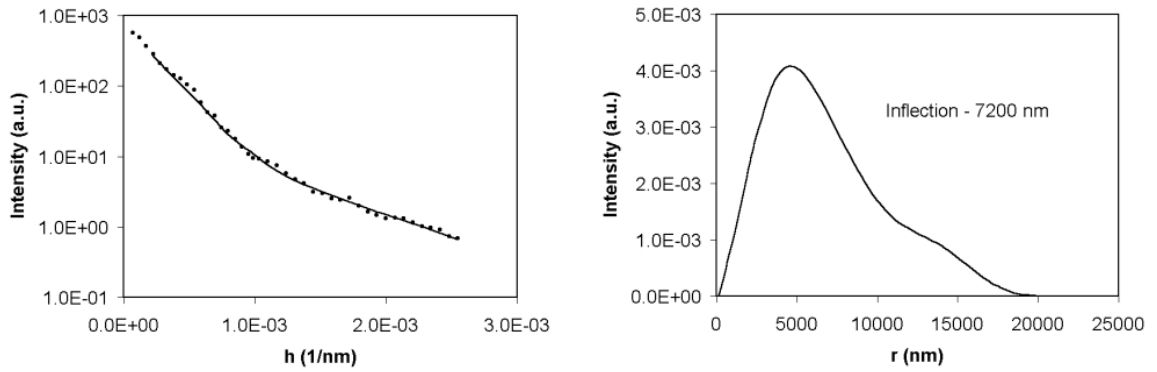


Figure 56. Run 20.  $D_{max} = 21000$ .  $NB = 6$ .  $\lambda = 2.5$ .

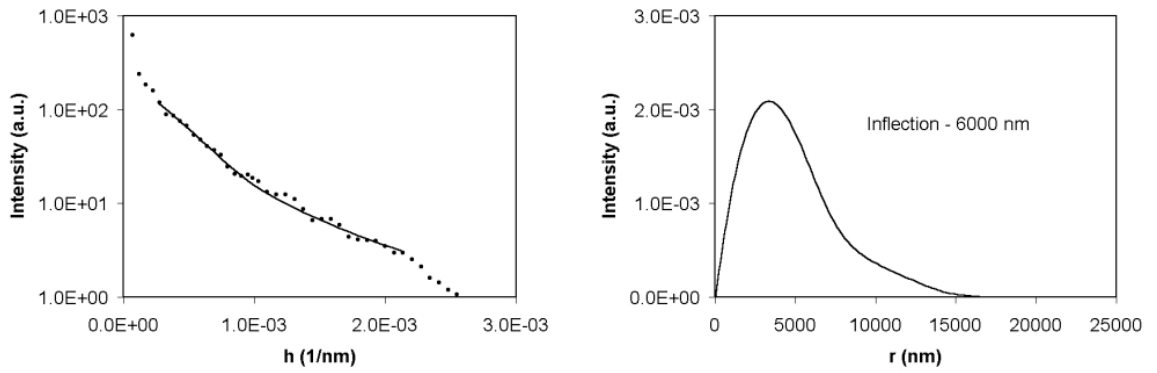


Figure 57. Run 21.  $D_{max} = 18000$ .  $NB = 5$ .  $\lambda = 3.0$ .

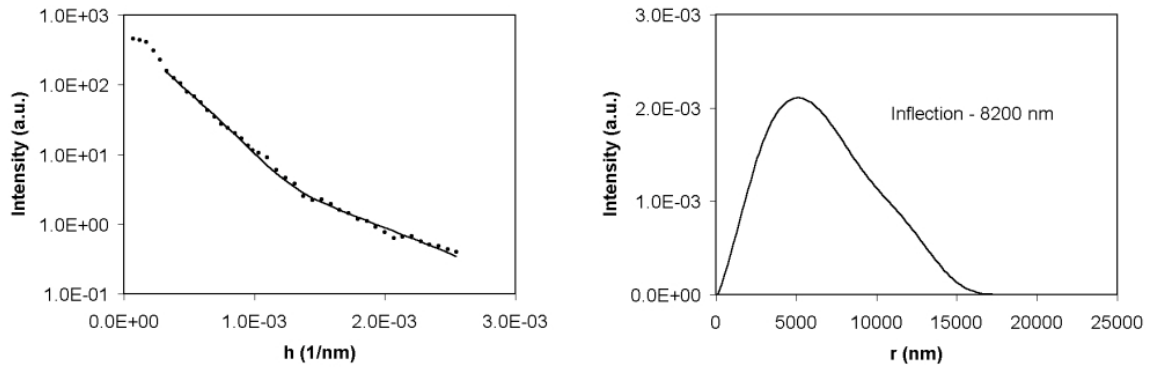


Figure 58. Run 22.  $D_{max} = 18000$ .  $NB = 6$ .  $\lambda = 3.5$ .

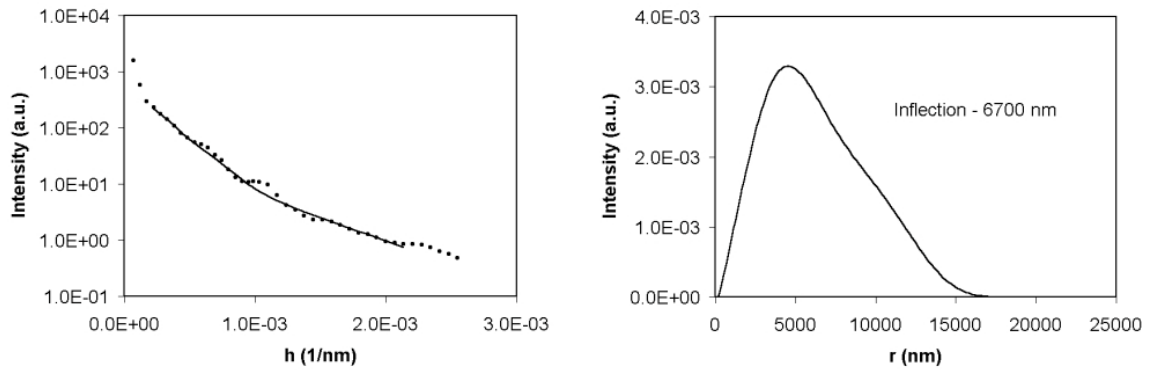


Figure 59. Run 23.  $D_{max} = 18000$ .  $NB = 5$ .  $\lambda = 2.5$ .

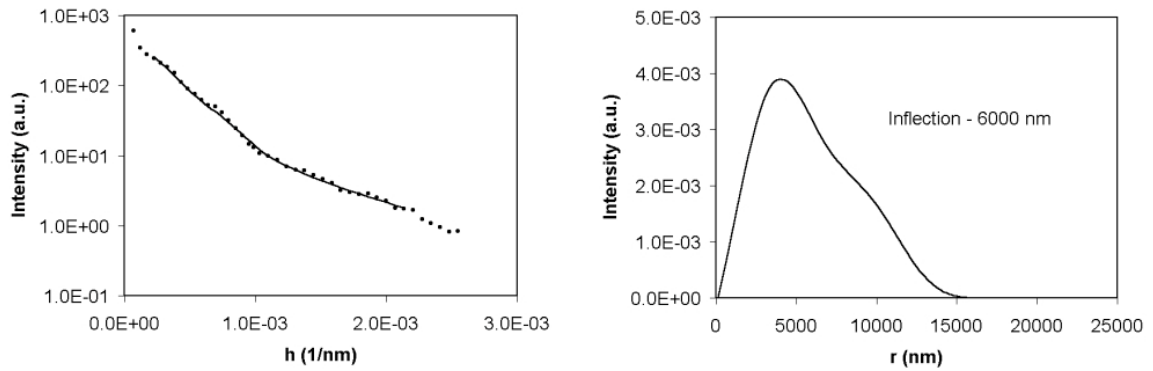


Figure 60. Run 24.  $D_{max} = 16500$ .  $NB = 5$ .  $\lambda = 3.5$ .

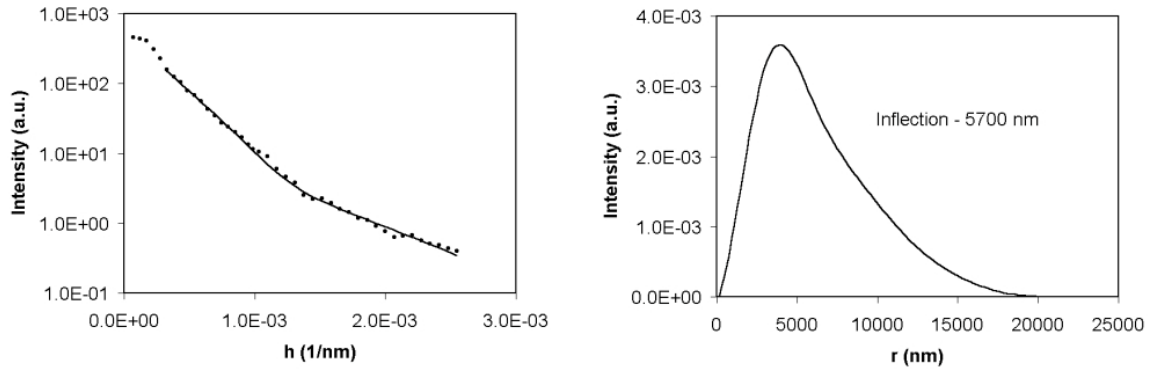


Figure 61. Run 25.  $D_{max} = 21500$ .  $NB = 7$ .  $\lambda = 2.5$ .

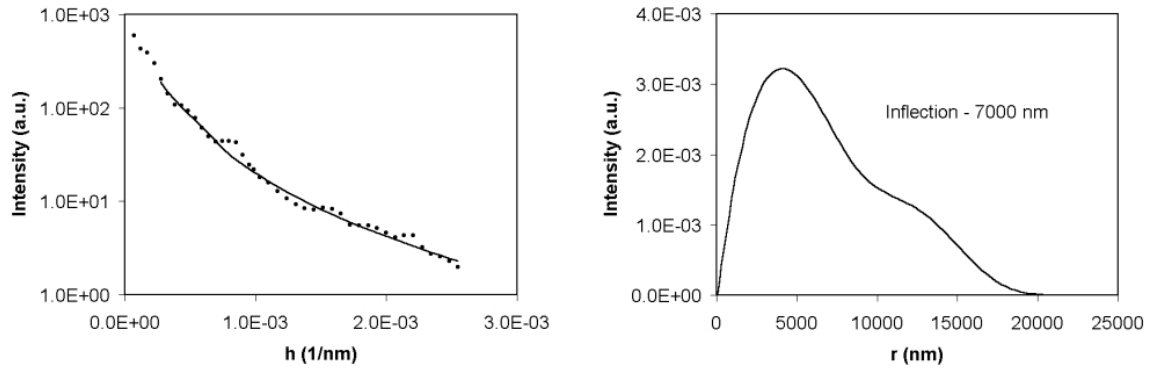


Figure 62. Run 26.  $D_{max} = 21500$ .  $NB = 5$ .  $\lambda = 0.0$ .

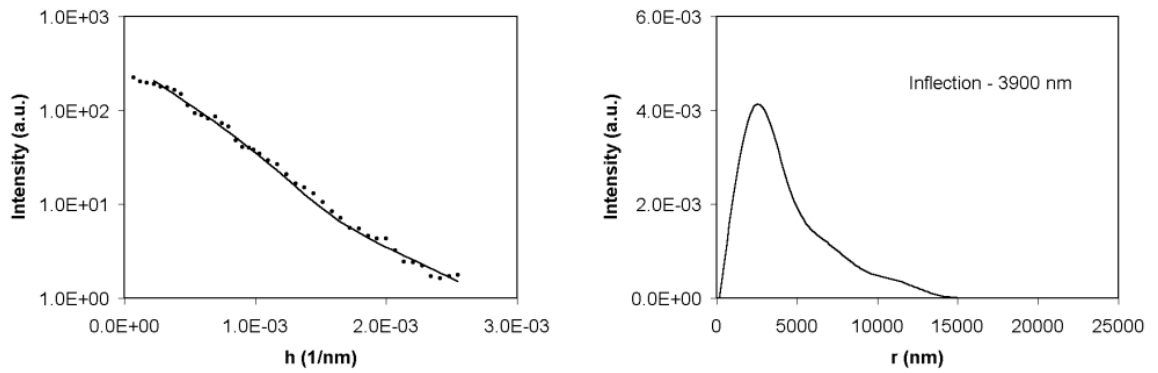


Figure 63. Run 27.  $D_{max} = 16000$ .  $NB = 7$ .  $\lambda = 3.5$ .

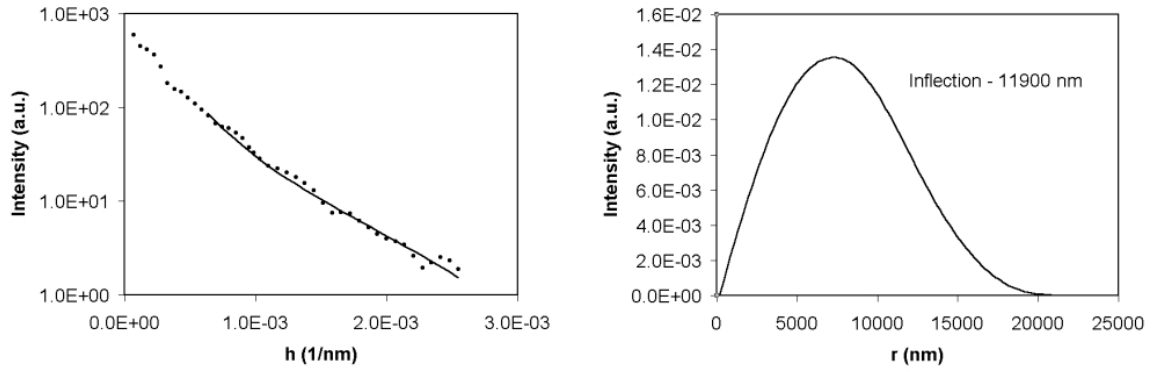


Figure 64. Run 28.  $D_{max} = 22000$ .  $NB = 5$ .  $\lambda = 2.0$ .

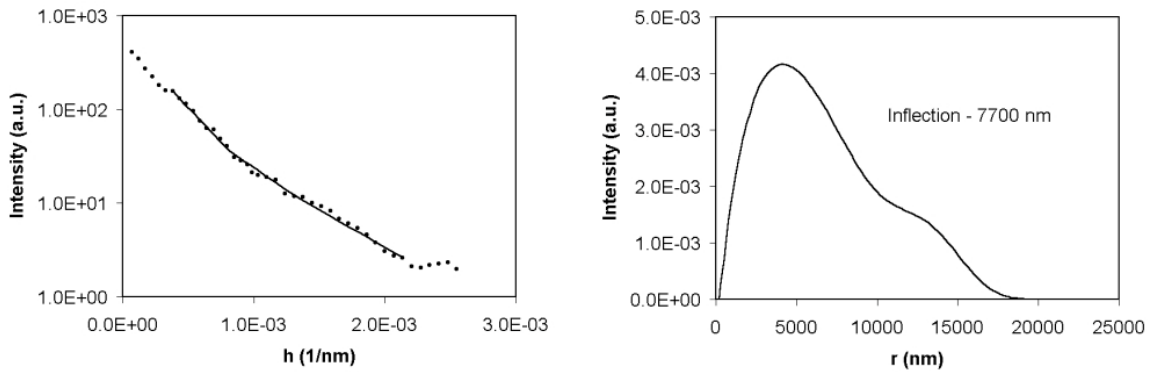


Figure 65. Run 29.  $D_{max} = 20000$ .  $NB = 6$ .  $\lambda = 1.5$ .

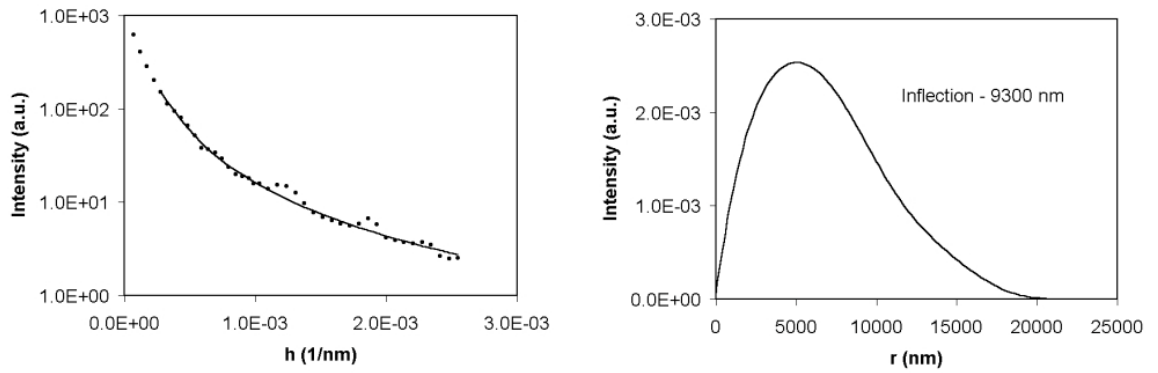


Figure 66. Run 30.  $D_{max} = 22000$ .  $NB = 6$ .  $\lambda = 3.0$ .

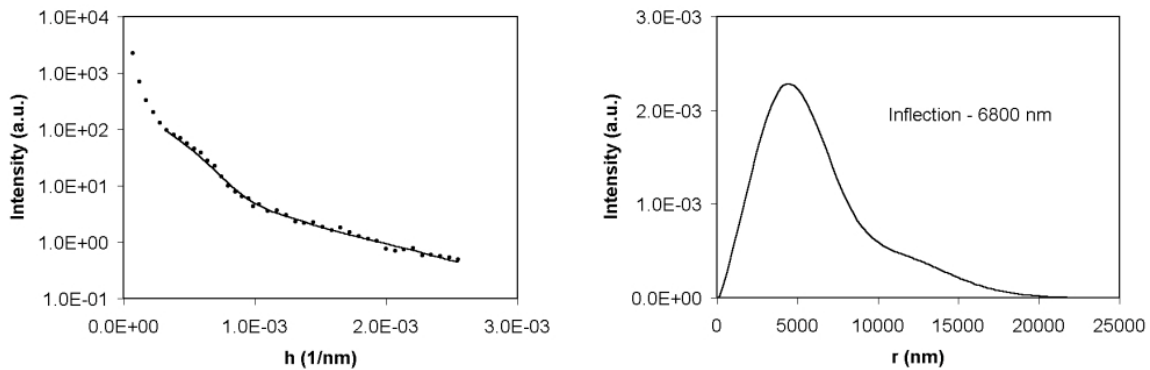


Figure 67. Run 31.  $D_{max} = 24000$ .  $NB = 6$ .  $\lambda = 2.5$ .

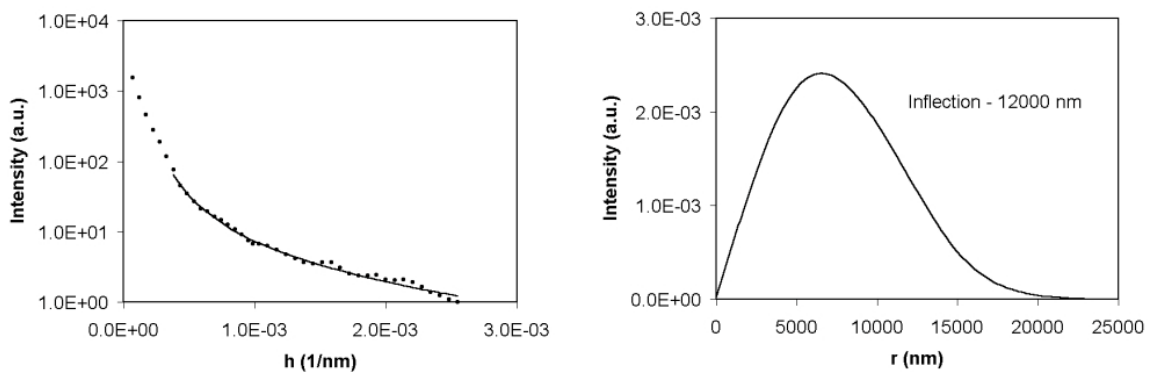


Figure 68. Run 32.  $D_{max} = 25000$ .  $NB = 5$ .  $\lambda = 2.5$ .

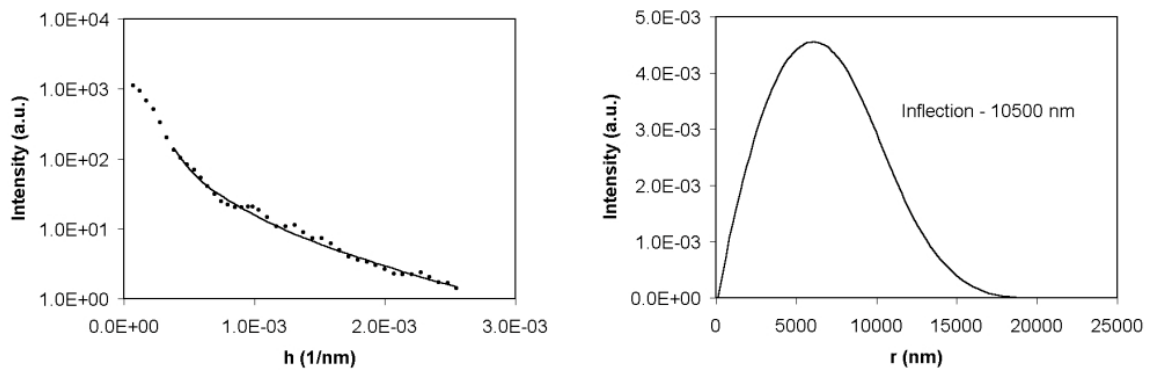


Figure 69. Run 33.  $D_{max} = 20000$ .  $NB = 5$ .  $\lambda = 3.0$ .

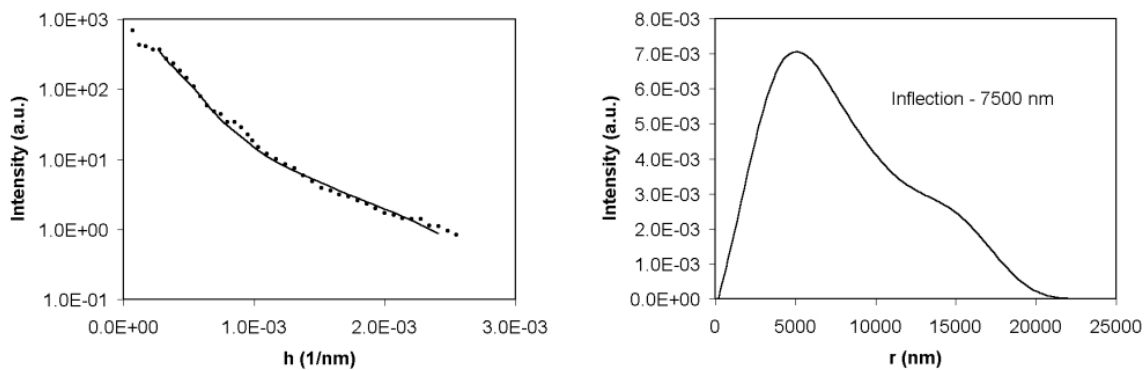


Figure 70. Run 34.  $D_{max} = 23000$ .  $NB = 6$ .  $\lambda = 3.0$ .

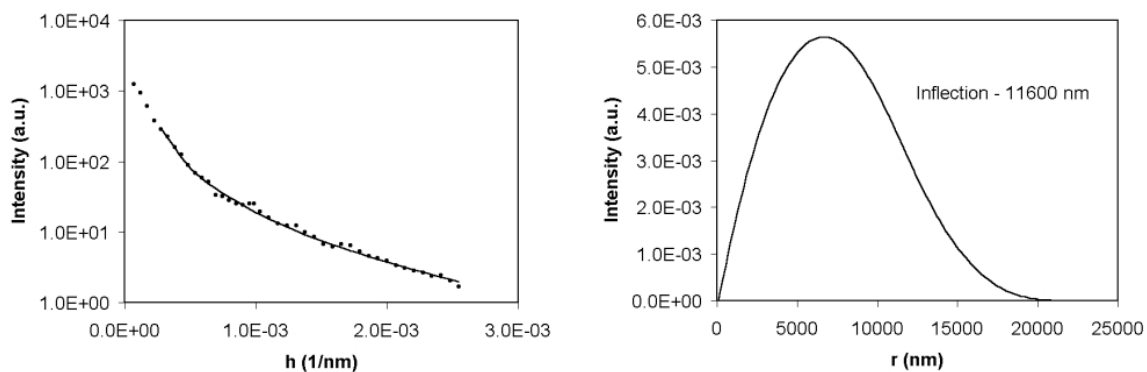


Figure 71. Run 35.  $D_{max} = 22000$ .  $NB = 5$ .  $\lambda = 2.5$ .

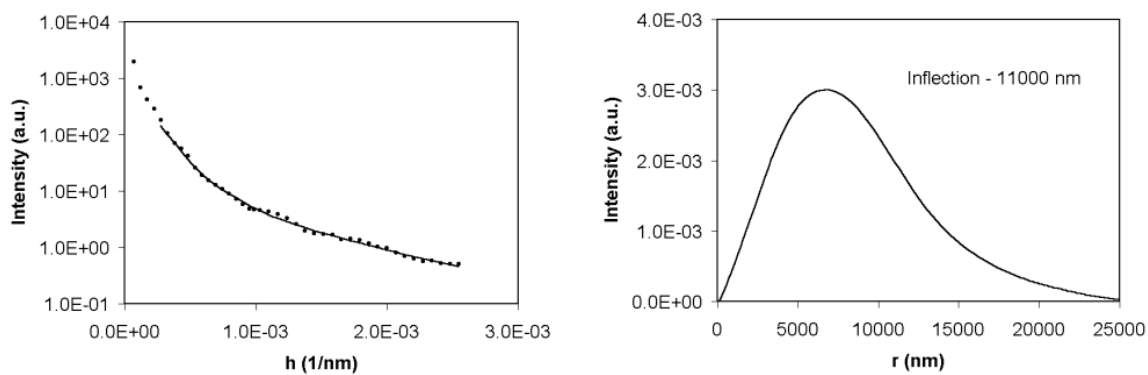


Figure 72. Run 36.  $D_{max} = 29000$ .  $NB = 7$ .  $\lambda = 2.5$ .

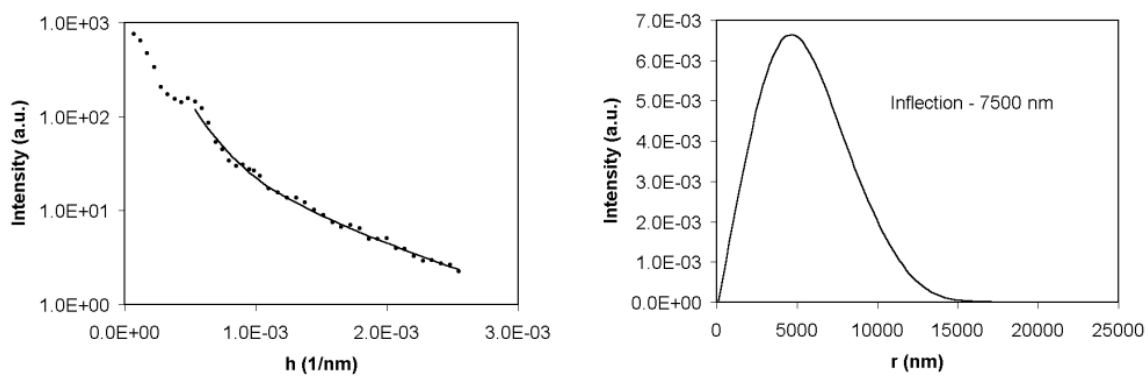


Figure 73. Run 37.  $D_{max} = 20000$ .  $NB = 5$ .  $\lambda = 2.5$ .

## 9.4 Experimental Procedure

### 9.4.1 CASI Alignment

1. Remove focusing optic, pinhole, and collimator from spatial filter.
2. Center target in beam path. Target should be at detector height.
3. Insert focusing optic. Adjust vertical and horizontal translational stages so beam is centered on target.
4. Insert pinhole. Adjust vertical and horizontal pinhole placement so beam shows no signs of interference appear on target. This is done by using the knobs on the spatial filter.
5. Attach collimator. Adjust pinhole placement again if interference appears.
6. Adjust first mirror such that the beam is at detector height at second mirror.
7. Remove all equipment in beam path between second mirror and detector.
8. Place iris on CASI mounting bar.
9. Center beam on iris using vertical and horizontal adjustments on second mirror.
10. Rotate CASI mount  $180^\circ$ .
11. If beam is not centered on iris, adjust mount and mirror until the beam stays centered on the iris when mount is rotated  $180^\circ$ .
12. Place target between optical rail and CASI.
13. Adjust beam height using second mirror.
14. Place large lens in first optical rail assembly.
15. Center beam on target by adjusting the vertical and horizontal position of the large lens.
16. Place wooden pinhole on optical rail between the two lens positions.
17. Place small lens in second optical rail assembly.
18. Center beam on target by adjusting the vertical and horizontal position of the small lens.
19. Attach adjustable height, aluminum pinhole to base of CASI.
20. Attach rotating sample holder to CASI mounting bar.
21. Use CASI software to center the detector on the beam (see CASI user manual for procedure and menu descriptions [32]).
22. Take a signature scan using CASI.
23. Use the  $\beta-\beta_0$  feature in the BRDF plot to check how the left and right halves of the beam compare.
24. If there is significant discrepancy between the halves, the pitch and yaw of the detector must be adjusted until the signature scan becomes acceptable. The pitch and yaw knobs are located on the side and bottom of the detector.
25. If significant improvement is not made adjusting the pitch and yaw, the procedure should be performed again. Cleaning the mirrors and lenses may also help.

### 9.4.2 Data Acquisition

1. Align CASI.
2. Create new directory using a yymmdd format (y – year, m – month, d – day)
2. Secure sample slide to rotating sample holder.
3. Adjust position of sample so that the slide is in the center of rotation. This is done by slightly rotating the mount and adjusting the CASI until the position of the beam on the sample does not change.
4. Adjust software settings to a sample scan (see CASI user manual [32]).
5. Input desired angular range, aperture size, and angular increment. Angular increment should be small enough to ensure no holes exist in the scan. This work measured the signal from 0.3 to 15 degrees in 0.1 degree increments.
6. Take a total signal measurement.
7. Re-centering the receiver will generally not be necessary. Using current receiver position as center should be used when queried.
8. Begin data acquisition, saving file when prompted.

### 9.4.3 Tendon Fixation

The following should be performed in a hood, with proper protective clothing.

1. Pour 45 mL of 0.1M phosphate buffered saline (PBS) into loading apparatus.
2. Tie suture material to each end of the tendon, making sure enough suture is available on each end for attaching the tendon to the post and weights.
3. Secure tendon in loading apparatus. Thread suture through pulley.
4. Apply desired amount of weight.
5. Wait 10 minutes for the tendon to stop stretching, and verify the tendon is securely fastened.
6. Pour 5 mL of 25% grade I glutaraldehyde into apparatus.
7. Allow tendon to fix for 2.5 to 3 hours.
8. Pipette out the glutaraldehyde solution into a waste receptacle.
9. Add 50 mL of 0.1M PBS.
10. Allow tendon to sit for 1 hour.
11. Pipette out the PBS into a waste receptacle.
12. Add 50 mL of 0.1M PBS.
11. Allow tendon to sit for 1 hour.
13. Pipette out the PBS into a waste receptacle.
14. Remove tendon from apparatus.
15. Place tendon in 50 mL PBS bath overnight.
16. Remove tendon from PBS bath, and place in 10% formalin solution.
17. Deliver tendon to histology lab for sectioning.

*Note: It is recommended that fixation be done at refrigerated temperatures if possible. This stops the glutaraldehyde from polymerizing and degrading the quality of the fixation. Performing the above at room temperatures yielded no problems for our purposes.*